



The Unusual Brightness Phase Curve of (65803) Didymos

P. H. Hasselmann¹ , V. Della Corte², P. Pravec³ , S. Ieva¹ , I. Gai⁴, D. Perna¹ , J. D. P. Deshapriya¹ , E. Mazzotta-Epifani¹ , E. Dotto¹ , A. Zinzi^{5,6} , G. Poggiali^{7,8} , I. Bertini⁹ , A. Lucchetti¹⁰ , M. Pajola¹⁰ , J. Beccarelli¹⁰, M. Dall'Ora² , J.-Y. Li¹¹ , S. L. Ivanovski¹² , A. Rossi¹³ , J. R. Brucato⁷ , C. A. Thomas¹⁴ , O. Barnouin¹⁵ , J. M. Sunshine¹⁶ , A. S. Rivkin¹⁷ , M. Amoroso⁵, A. Capannolo^{18,19}, S. Caporali⁷, M. Ceresoli¹⁹, G. Cremonese¹⁰, R. T. Daly¹⁵ , G. Impresario⁵, R. Lasagni-Manghi⁴, M. Lavagna¹⁹, D. Modenini⁴, E. E. Palmer¹¹ , P. Palumbo⁹, S. Pirrotta⁵, P. Tortora⁴, M. Zannoni⁴, and G. Zanotti¹⁹

¹ INAF-Osservatorio Astronomico di Roma, Monte Porzio Catone, Italy; pedro.hasselmann@inaf.it

² INAF-Osservatorio Astronomico di Capodimonte, Naples, Italy

³ Astronomical Institute, Academy of Sciences of the Czech Republic, Ondřejov, Czech Republic

⁴ Alma Mater Studiorum—Università di Bologna, Dipartimento di Ingegneria Industriale, Forlì, Italy

⁵ Agenzia Spaziale Italiana, Via del Politecnico, 00133, Rome, Italy

⁶ Space Science Data Center, ASI, Rome, Italy

⁷ INAF-Osservatorio Astrofisico di Arcetri, Florence, Italy

⁸ LESIA, Observatoire de Paris-Meudon, Meudon, Île-de-France, France

⁹ Università degli Studi di Napoli “Parthenope”, Naples, Italy

¹⁰ INAF-Osservatorio Astronomico di Padova, Padova, Italy

¹¹ Planetary Science Institute, Tucson, AZ, USA

¹² INAF-Osservatorio Astronomico di Trieste, Trieste, Italy

¹³ IFAC-CNR, Sesto Fiorentino, Firenze, Italy

¹⁴ Department of Physics and Astronomy, Northern Arizona University, Flagstaff, AZ, USA

¹⁵ Johns Hopkins University Applied Physics Laboratory, Laurel, MD, USA

¹⁶ University of Maryland, Department of Astronomy and Department of Geology, College Park, MD, USA

¹⁷ University of Maryland, Department of Astronomy, MD, USA

¹⁸ ISAE-SUPAERO, Université de Toulouse, Toulouse, France

¹⁹ Politecnico di Milano, Dip. di Scienze e Tecnologie Aerospaziali, Milano, Italy

Received 2023 September 27; revised 2024 February 16; accepted 2024 February 16; published 2024 April 3

Abstract

On 2022 September 26, NASA's Double Asteroid Redirection Test (DART) successfully hit Dimorphos, the smaller companion of the binary system formed with the asteroid (65803) Didymos. Both the binary system and the impact event were imaged by the Light Italian Cubesat for Imaging of Asteroids, detached from DART 15 days before the impact. Images from the onboard LUKE red, green, and blue camera together with ground-based observations enabled the reconstruction of Didymos's brightness phase curve, with phase angles ranging from 2.35° to 107.7° . The opposition effect regime was studied using the exponential-linear equation, the “Shevchenko” function and the linear-by-parts model while the IAU-official HG1G2 magnitude system was applied to the full phase curve. The opposition effect indicates an unusual asteroid surface for an S type, with characteristics similar to M-type asteroids. While the HG1G2 parameters from the full phase curve place Didymos well among asteroids of the taxonomic C complex. Didymos's phase curve parameters when compared to near-Earth asteroids are very close to the Q type (1862) Apollo, indicating possible depletion of fine submicrometric grains through resurfacing. Didymos's geometric albedo (0.15 ± 0.01) is reported to be 30%–45% smaller than the average geometric albedo for near-Earth S types (0.26 ± 0.04). We propose that Didymos might be an LL ordinary chondrite analog containing albedo-suppressing, shock-darkened/impact melt minerals that have undergone resurfacing processes in the past. A comparison with meteorites indicates that, less likely, Didymos could also contain materials analog to carbon-bearing brecciated L3 ordinary chondrites.

Unified Astronomy Thesaurus concepts: Asteroids (72); Asteroid surfaces (2209); Phase angle (1217); Near-Earth objects (1092); Photometry (1234); RGB photometry (1397)

1. Introduction

The NASA Double Asteroid Redirection Test (DART) mission successfully accomplished the first planetary defense test on 2022 September 26 when it intentionally impacted Dimorphos, the secondary asteroid of the (65803) Didymos binary system (Daly et al. 2023), demonstrating the capabilities of the kinetic redirection technique. Dimorphos was hit by

DART with a velocity of 6.145 km s^{-1} , reducing the orbital period by 33 ± 1 minutes (Thomas et al. 2023) and producing a complex ejecta plume (Dotto et al. 2024). The first seconds to minutes into the event were witnessed by both the Light Italian Cubesat for Imaging of Asteroids (LICIACube) Explorer Imaging for Asteroid (LEIA) and LICIACube Unit Key Explorer (LUKE) cameras on board the 6U CubeSat LICIACube developed by the Italian Space Agency (Dotto et al. 2021). The CubeSat detached from the DART spacecraft 15 days before the impact, achieving the required safe distance and position to study the event. Both cameras captured several hundred images during the flyby maneuver, with the closest approach (CA) happening 167 s after the impact, 57 km from

the binary. The LICIACube disk-resolved data have the largest phase angle coverage, ranging from 43° to 118° .

The disk-integrated brightness phase curve of asteroids is the radiative expression of the collective properties of atmosphereless granular surfaces scattering the solar incidence radiation with respect to the phase angle (Bowell & Lumme 1979; Lumme & Bowell 1981; Li et al. 2015). The latter is the angle between the solar, target, and observer positions. Similarly to asteroid spectra, phase curves carry indirect information on the material reflectivity, grain size, surface irregularities, and granular packing. Such information is partially decoded through morphological parameters obtained from empirical or semiempirical models (Bowell et al. 1989; Hapke 1993; Kaasalainen et al. 2003; Muinonen et al. 2010) and also their intercomparison with parameters, composition, and spectral types from other asteroids or meteoritic samples (Belskaya & Shevchenko 2000; Mahlke et al. 2021; Ieva et al. 2022a; Alvarez-Candal et al. 2022). Furthermore, the phase curve characterization is of ultimate importance for the determination of absolute magnitude, a crucial parameter to estimate the diameter of atmosphereless small bodies from disk-unresolved observations (Harris & Lagerros 2002; Stuart & Binzel 2004).

Didymos is an Apollo-class near-Earth asteroid (NEA) of equivalent ellipsoid shape of $851 \times 849 \times 620 \text{ m}^3$ (Daly et al. 2023; Palmer et al. 2023) discovered by the Spacewatch survey in 1996 (Rabinowitz 1991) and the primary asteroid of a binary system. The presence of a satellite, later named Dimorphos, was discovered by light-curve and radar observations (Pravec et al. 2003), with a preimpact orbital period recently updated to 11.92 hr (Scheirich & Pravec 2022). Originally assigned as an Xk type (Binzel et al. 2004), further VIS-IR spectroscopic observations and analysis led Didymos to be reclassified as an S type (de León et al. 2006, 2010) and improved to a meteoritical correspondence related to L/LL ordinary chondrites (Dunn et al. 2013). Recent observations have also shown that Didymos displays a subtle rotational spectral variation possibly associated with locally strong or widespread weak inhomogeneities (Ieva et al. 2022b).

In the present study, the disk-integrated phase curve of Didymos is composed from previously published *R* Cousins and Sloan Digital Sky Survey (SDSS) *r'* ground-based observations (Kitazato et al. 2004; Pravec et al. 2006, 2022) and new data from the LUKE red, green, and blue (RGB) Bayer pattern camera. Didymos remained observable during the LICIACube postimpact flyby, while Dimorphos was highly obscured by the ejecta plume. Data information and their conversion to *R* Cousins are presented in Section 2. Deriving the apparent albedo, removing other photometric effects from LUKE images, and combining ground-based and LICIACube observations are dealt in Section 3. The final phase curve spans from 2.35° to 107.7° in phase angle, covering regimes from near opposition effects (OEs) to surface macroscale roughness and topographic effects (Li et al. 2015). In Section 4, parameters obtained through standard HG and HG1G2 magnitude systems (Muinonen et al. 2010) are compared to other cataloged parameters for asteroids of diverse spectral type. The OE is also studied using the exponential-linear equation (Muinonen et al. 2009), the “Shevchenko” function (Shevchenko 1996), and the linear-by-parts model (Déau et al. 2016), then compared in similar fashion. In Section 4.3, we compared Didymos’s phase curve parameters to other available

information on NEAs of similar diameter range. In Section 5, we discuss the findings and possible interpretations for reconciling Didymos’s spectral type and its phase curve. We explore the hypothesis of shock darkening and impact melts suppressing Didymos’s albedo from a brighter ordinary chondrite composition. We also point to a less likely possibility that Didymos could also contain carbon-bearing brecciated composition as albedo suppression content but at a much lesser extent.

2. Data

2.1. Ground-based Observations

This asteroid binary system has been the target of observational campaigns during the last 20 yr. Didymos, then provisionally designated (65803) 1996 GT, was observed during the northern observational window of 2003 November–December by Kitazato et al. (2004) and Pravec et al. (2006). Kitazato et al. acquired light curves of Didymos ranging from 2.35° to 40° of phase angle at the K.3T robotic telescope of the Japanese Kiso Observatory in the *R* band. Multiband observations were also conducted from the same observatory at the beginning of 2003 December. They reported color indexes $U - B = 0.21 \pm 0.03$, $B - V = 0.79 \pm 0.02$, $V - R = 0.458 \pm 0.009$, and $V - I = 0.820 \pm 0.009$ from the results of *UBVRI* photometry. Pravec et al. (2006) acquired light curves during 6 nights in November of the same year as well, leading to the detection of its binarity and measurement of its rotational and orbital periods. Once the secondary asteroid of the system was selected as the target of the DART mission, a light-curve observational campaigns was conducted from varied telescopes between 2015 and 2021 in order to improve Dimorphos’s orbital period and body elongation (Pravec et al. 2022). This campaign then provided reduced magnitudes for phase angles spanning from 3.4° to 44.4° that make up the part of our phase curve reconstruction. Reduced magnitudes $m_{(1,1a)}$ are defined as the apparent logarithmic flux of the object surface illuminated by the solar irradiance at 1 au and observed from a distance of 1 au. “Reduced” means they have been corrected from the primary’s rotational period and mutual occultation events between the primary and secondary bodies. Thus, this magnitude corresponds to the mean brightness for the whole system. In particular, the observations between 2017 February 23 and March 1 only have one reduced magnitude reported for the entire period. This magnitude was derived for $\alpha = 17.9^\circ$, but we chose to represent the 5 observation nights by a streak of three stars: the beginning, middle, and end of the phase angle range from 16.4° to 19.3° . These weeklong observations were obtained in the PS1 filter at the Very Large Telescope (VLT) and converted to SDSS *r'* by the observer. These reduced magnitudes are then combined with the LICIACube photometric data to complete the phase curve down to the small phase angles. Table 1 provides a summary of the published light-curve-corrected reduced magnitudes and information on the observation nights such as cross sections, phase angle, and subobserver and subsolar latitudes.

Reduced magnitudes in Pravec et al. (2022) are mainly acquired in two red filter systems: Cousins *R* and SDSS *r'*. Lupton et al. (2004) derives the following conversion equation from SDSS $(r - i)'$ color to Cousins *R* using Landolt star

Table 1Reduced Magnitudes $m_{(1,1,\alpha)}$, Magnitude Uncertainties δm , Total Cross Section S , Didymos Cross-section Ratio S_{didy}/S , and Other Observational Information for the Ground-based Observations from 2003 to 2021

Date (1)	α (deg) (2)	$m_{(1,1,\alpha)}$ (3)	δm (4)	S (km ²) (5)	S_{didy}/S (6)	lat _{subobs} (deg) (7)	lat _{subsolar} (deg) (8)	Red Band (9)	Station/ Telescope (10)
Pravec et al. (2006, 2022)									
2003-11-20.9	19.0	18.642	0.01	0.3965	0.9582	-15.6	0.4	<i>R</i>	Ondrřejov
2003-11-22.0	16.7	18.572	0.01	0.3962	0.9589	-13.5	0.7	<i>R</i>	Ondrřejov
2003-11-27.9	7.1	18.196	0.01	0.3865	0.9586	-4.2	2.1	<i>R</i>	Ondrřejov
2003-11-30.0	4.9	18.092	0.01	0.3879	0.9585	-1.7	2.5	<i>R</i>	Ondrřejov
2003-12-16.9	7.4	18.204	0.015	0.3980	0.9570	8.6	6.0	<i>R</i>	Ondrřejov
2003-12-18.9	8.5	18.223	0.015	0.4027	0.9571	8.3	6.5	<i>R</i>	Ondrřejov
2021-01-20.2	26.2	18.819	0.019	0.3975	0.9580	15.5	13.0	SDSS <i>r'</i>	TNG
2017-03-31.1	3.4	18.040	0.03	0.3971	0.9559	12.2	9.6	SDSS <i>r'</i>	WHT
2017-04-01.3	3.8	18.014	0.03	0.4046	0.9577	12.1	7.1	SDSS <i>r'</i>	VLT
2017-04-02.3	4.3	18.045	0.03	0.4061	0.9566	12.2	9.5	SDSS <i>r'</i>	VLT
2019-01-31.4	26.2	18.880	0.02	0.3982	0.9594	12.4	12.6	SDSS <i>r'</i>	DCT
2019-02-02.2	25.3	18.861	0.02	0.3946	0.9576	12.5	12.7	SDSS <i>r'</i>	Magellan
2020-12-17.4	44.4	19.509	0.02	0.3987	0.9560	13.0	11.8	SDSS <i>r'</i>	LDT
2020-12-20.5	43.2	19.453	0.02	0.3837	0.9550	13.4	11.9	SDSS <i>r'</i>	LDT
2020-12-23.4	42.0	19.396	0.02	0.3885	0.9561	13.5	12.0	SDSS <i>r'</i>	LDT
2021-01-08.5	33.9	19.117	0.02	0.3909	0.9574	14.5	12.7	SDSS <i>r'</i>	LDT
2021-01-09.4	33.3	19.091	0.02	0.3999	0.9586	14.7	12.6	SDSS <i>r'</i>	LDT
2021-01-10.4	32.7	19.089	0.02	0.3924	0.9566	14.8	12.8	SDSS <i>r'</i>	LDT
2021-01-14.4	30.2	19.021	0.02	0.3954	0.9582	15.1	12.8	SDSS <i>r'</i>	LDT
2021-03-06.3	11.1	18.388	0.02	0.4057	0.9588	16.7	12.7	SDSS <i>r'</i>	LDT
2017-02-23.3-2017-03-01.3 ^a	17.9	18.559	0.02	0.3926-0.3981	0.9568-0.9586	10.5	10.9	<i>PSI</i>	<i>VLT</i>
Kitazato et al. (2004)									
2003-12-03.5	2.35	17.980	0.03	0.3897	0.9579	1.2	3.3	<i>R</i>	K.3T
2003-11-23.0	13.3	18.550	0.03	0.3880	0.9584	-11.6	0.9	<i>R</i>	K.3T
2003-11-17.0	27.6	18.930	0.03	0.4104	0.9581	-14.6	0.5	<i>R</i>	K.3T
2003-11-13.5	39.9	19.270	0.03	0.4380	0.9585	-22.7	-1.4	<i>R</i>	K.3T

Note. α —phase angle; lat—latitude. Italics indicate sequence of observations represented by a single phase angle.^a Phase angle for the 5 nights ranges from 16.4° to 19.3°, but the reduced magnitude is only derived for the central $\alpha = 17.9^\circ$.

absolute magnitudes:

$$R = r' - 0.2936 \cdot (r - i)' - 0.1439. \quad (1)$$

Assuming the i' magnitude and associated phase spectral reddening coefficient for the whole system are both unknown, we selected magnitudes in both red systems obtained between 2° and 20° phase angles and applied to each a linear fit in order to calculate the y-intercept values. All linear parameters are derived using ordinary least-squares (OLS) regression implemented in the Python 3.9 library statsmodel (Seabold & Perktold 2010). The OLS finds the best-fitting line by minimizing the residuals associated with the data points. From the y-intercepts and the equation above we estimated the color $(r - i)' = 0.073 \pm 0.122$, and we offset all SDSS magnitudes accordingly. K. Kitazato's *R*-band observations are also affected by an offset (K. Kitazato, private communication) and thus solved by a similar approach. We derived a magnitude slope differential factor of 0.04 mag deg⁻¹ and offset of -0.03 for K. Kitazato's observations. The result is shown in Figure 1. The final linear absolute magnitude and linear phase slope coefficient are 17.93 ± 0.02 and 0.035 ± 0.001 , respectively.

2.2. LUKE Camera

The DART spacecraft successfully impacted Dimorphos at precisely 23h14m24.187 s UT, fulfilling its goal to carry a deflection experiment on an asteroid. The multiplicative effect

of the momentum transfer is expressed by the so-called parameter β , and for the DART experiment, it is estimated to be between 2.2 and 4.9 (Cheng et al. 2023). A $\beta \gg 1$ means that a highly effective deflective action is achieved and that significant momentum was transferred through the escaping ejecta plume. The early evolution of this ejecta plume, as well as the binary system, was observed by the LUKE camera. The optical system consists of a front-illuminated CMOS CMV2000 detector equipped with an RGB Bayer pattern filter (Poggiali et al. 2022). The CCD has the characteristic pixel size of 5.5 μm and dimensions of 1088 \times 2048 pixels. LUKE obtained triplets of images at 3 frames per second with exposure times ranging from 0.2 ms to 0.5 s. The triplets were obtained in a short time sequence and contained short-, middle-, and high-exposure acquisitions. The LUKE observations started 28 s after the impact and continued until 242 s after that. From that point, the binary system brightness was below the instrument detection level. The CA happened at 23h17m11.508 s UT on the same day, roughly 2 minutes and 53 s after the impact time. However, due to uncertainties associated with the CubeSat pointing, only Didymos is visible within the LUKE field of view at the CA.

The LUKE images were originally obtained in digital number during the flight and radiometrically calibrated to radiance ($\text{Wm}^{-2} \text{nm}^{-1} \text{sr}^{-1}$) through a pipeline using both ground preflight measurements with a calibrated integrating sphere (an example of similar application to the BepiColombo/

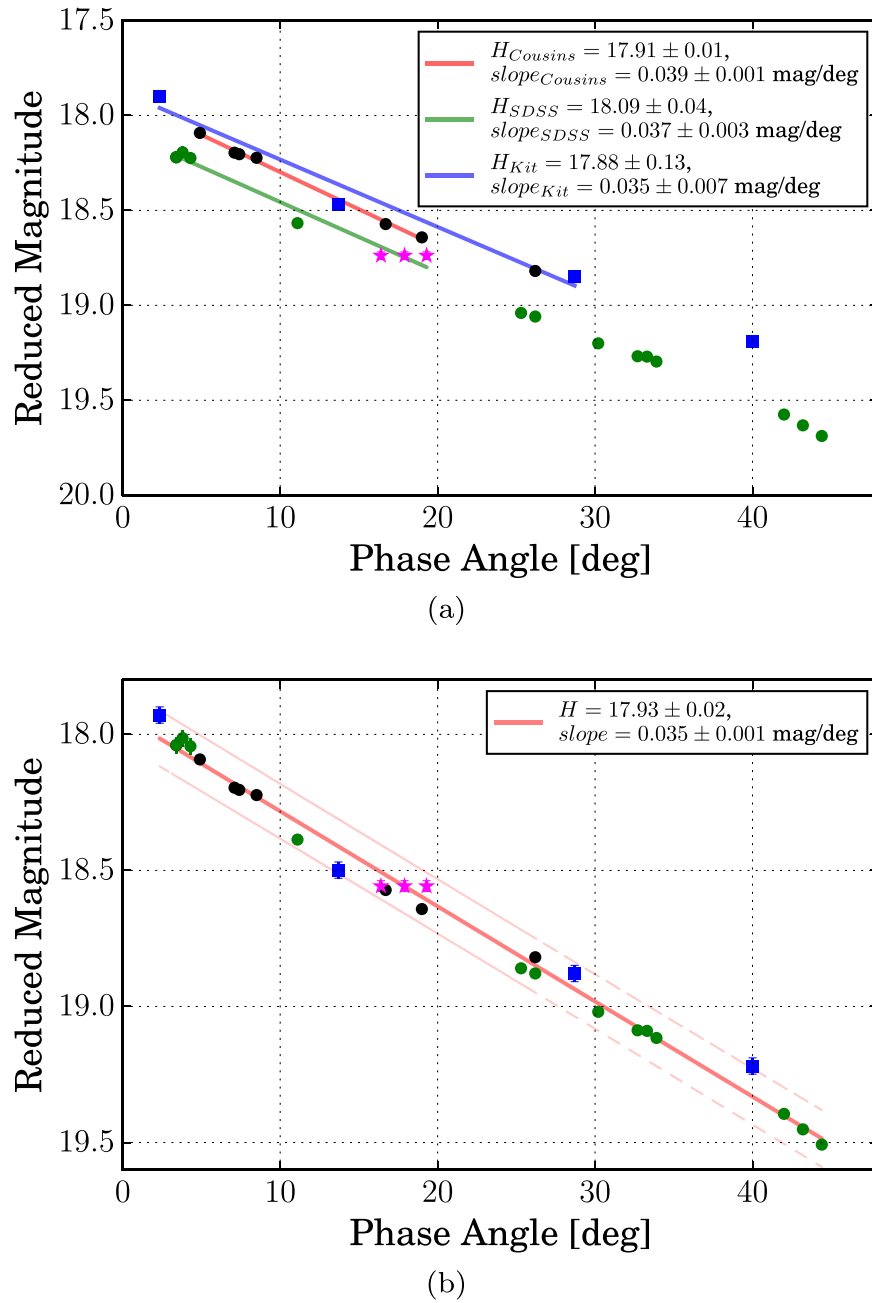


Figure 1. Ground-based reduced magnitudes of Didymos's binary system from 2003 to 2021. (a) Linear fit for SDSS r' and R Cousins magnitudes in between 2° and 20° phase angles and down to 30° for Kitazato et al. Color code: Pravec et al. SDSS r' magnitudes in green, Pravec et al. R Cousins magnitudes in black, Kitazato et al. R magnitudes in blue, and VLT magnitude observations between 2017 February 2 and March 1 in magenta are represented by a streak of three stars: the beginning, middle, and end of the observational period. (b) Total linear absolute magnitude and linear phase slope coefficient (light red line) for all ground-based magnitude data now converted to standard Cousins R . The dotted light red lines represent the 1σ uncertainty envelope.

SIMBIOSYS instrument in Da Deppo et al. 2014) and in-flight measurements of standard stars. This process involves eliminating the DARK signal and detector bias, which are determined through on-ground calibration, and accounting for the detector's response to incident light (Dotto et al. 2021; Poggiali et al. 2022). Finally, radiance factors were obtained by correcting the radiance by the solar irradiance integrated over RGB Bayer bandpasses.

The Bayer mosaic is a type of color filter array that arranges RGB color filters in a square grid on photosensors. This specific arrangement is commonly employed in most single-chip digital image sensors to generate color images. The filter

pattern consists of half green, one-quarter red, and one-quarter blue elements, and in the case of LUKE, it follows the RGGB pattern. Because each pixel records only one of three colors, the data from each pixel alone cannot fully define the red, green, or blue values; to obtain a complete color image, a demosaicking algorithm is employed to interpolate a set of complete red, green, and blue values for each pixel. The algorithm analyzes the neighboring pixels of corresponding colors to estimate values for a specific pixel. For the LUKE images, we employed the algorithm by Menon et al. (2007). Uncertainties due to the instrumental radiometrics are estimated to be about 20%, as reported by the ASI-APS/LICIACube Team. RGB Bayer

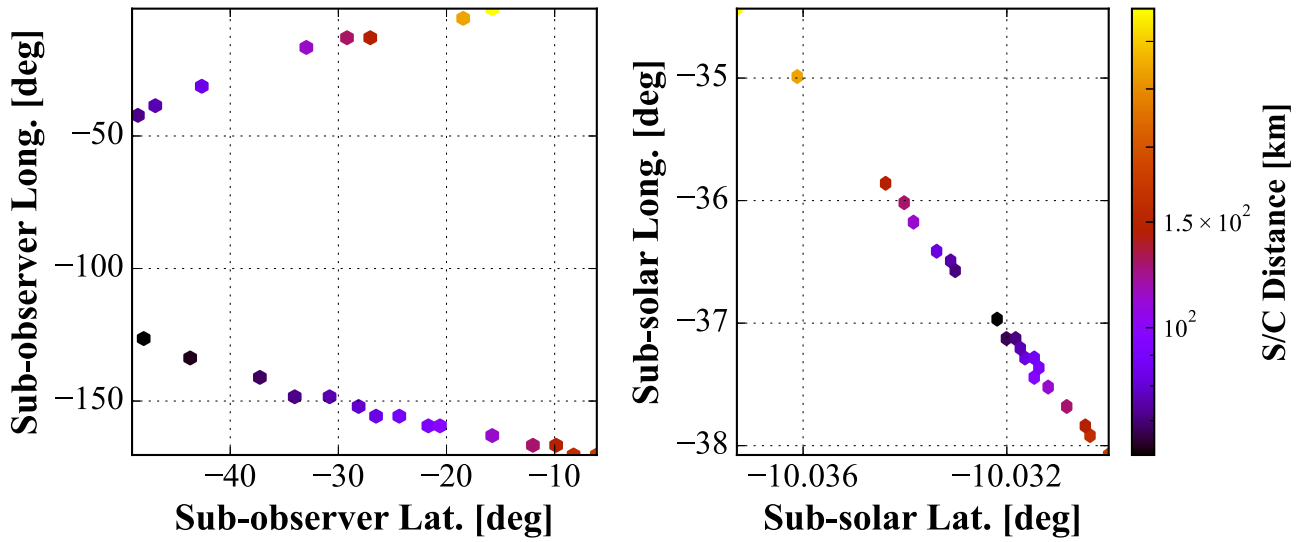


Figure 2. The (left) subobserver and (right) subsolar points in local Didymos latitude and longitude for the selected LUKE image. The dots are colored according to the spacecraft distance (km) in natural logarithm scale.

apparent magnitudes were then converted to Cousins R using the conversion presented by Park et al. (2016) and corrected using the zero-point reported in the pipeline:

$$R = R_b + 0.051 \cdot (B_b - G_b) + 0.469 \cdot (G_b - R_b) - \mathbf{0.826}, \quad (2)$$

where the subscript b represents Bayer magnitudes. LUKE’s zero-point for converting RGB to Cousins R is emphasized in bold.

Finally, we selected for our analysis short-exposure images of Didymos where the full disk is not saturated, overcome by the plume signal, or too close to the image limb. The exposure time varies between 0.2 and 0.7 ms, and the images were acquired 112 to 194 s after the DART impact time. The subobserver and subsolar points indicate that the observations cover mostly the southern hemisphere during the flyby (see Figure 2). Phase angles ranged from 43.3° to 107.7° . Information on all selected images is shown in Table 2.

2.3. Ancillary Data: Shape Model and NAIF/SPICE Kernels

We computed the asteroids’ cross section using the shape model of Didymos and Dimorphos and the astrometrical ephemeris made available by the DART and LICIAcube teams. The Dimorphos shape model was reconstructed from Didymos Reconnaissance and Asteroid Camera for Optical Navigation (DRACO; Fletcher et al. 2022) images obtained before the impact using the stereo-photoclinometry technique (Daly et al. 2023, 2024). We rely on the latest version “v003” of the Digital Terrain Model (DTM) shrunk to 49k facets, an equivalent horizontal spatial resolution of 1.9 m. The Didymos shape model was reconstructed in a similar manner by Palmer et al. (2022, 2023). Again, a DTM shrunk to 49k facets of the latest version “v003,” with an equivalent horizontal spatial resolution of 9.3 m, was used for cross-section calculation.

The SPICE software provided by the Navigation and Ancillary Information Facility (NAIF) from the Jet Propulsion Laboratory is a tool for computing relative position, instrument framing, and rotational states for solar system bodies and spacecraft within the solar system (Acton 1996; Acton et al. 2018). The NAIF/SPICE astrometrical data of LICIAcube

Table 2
Short-exposure LUKE I2 Images Selected for Analysis

Image (1)	UT (2)	exptime [ms] (3)	Δ [km] (4)	α [deg] (5)	$T+$ [s] (6)
1664234177	23:16:16	0.5	340.1	53.7	112
1664234189	23:16:28	0.5	267.9	52.3	124
1664234210	23:16:49	0.2	144.8	47.2	145
1664234213	23:16:52	0.4	128.1	45.9	148
1664234216	23:16:55	0.3	112.1	44.6	151
1664234222	23:17:01	0.2	82.9	42.6	157
1664234224	23:17:03	0.3	74.7	42.8	159
1664234225	23:17:04	0.2	71.1	43.3	160
1664234234	23:17:13	0.2	60.5	67.0	169
1664234235	23:17:14	0.5	62.3	70.7	170
1664234237	23:17:16	0.2	67.5	77.8	172
1664234238	23:17:17	0.5	70.7	80.9	173
1664234239	23:17:19	0.3	74.7	84.0	174
1664234240	23:17:19	0.2	78.3	86.4	175
1664234241	23:17:20	0.7	82.5	88.7	176
1664234242	23:17:21	0.3	86.9	90.8	177
1664234243	23:17:22	0.2	91.5	92.8	178
1664234244	23:17:23	0.7	96.3	94.5	179
1664234247	23:17:26	0.3	111.5	98.7	182
1664234250	23:17:29	0.5	127.6	101.9	185
1664234253	23:17:32	0.5	144.2	104.2	188
1664234256	23:17:35	0.5	161.2	106.2	191
1664234259	23:17:38	0.3	178.5	107.7	194

Note. UT—universal time; exptime—exposure time; Δ —spacecraft distance to Didymos; α —phase angle; $T+$ —seconds after the impact. The nearest image to the CA is shown in bold.

were reconstructed using telemetry and the assistance of LUKE images by the Italian Investigation Team coordinated by the Italian Space Agency (ASI; Capannolo et al. 2021). The binary system orbital and rotational states were refined using radar, light-curve, and DRACO images by the DART Investigation Team and made available as NAIF/SPICE kernels as well. NAIF/SPICE LICIAcube and DART kernels will be publicly available.²⁰

²⁰ <https://naif.jpl.nasa.gov/pub/naif/>

Table 3

Solar Irradiance and Apparent Solar Magnitudes Associated with the LUKE Bands

Band Λ	λ	$J_{\Lambda 0}$	M_{\odot}
(1)	(2)	(3)	(4)
R	617.52 nm	1.6497 W m ⁻² nm ⁻¹	-26.64
G	544.57 nm	1.8331 W m ⁻² nm ⁻¹	-26.76
B	474.99 nm	1.8353 W m ⁻² nm ⁻¹	-26.76

The shape models and NAIF/SPICE astrometrical files enable one to position the surface of the asteroid and the spacecraft in the 3D solar system frame and compute their relative trajectory and rotational velocities. NAIF/SPICE files also carry information on the instrument's field of view, pointing, and position in the spacecraft bus frame. All these data are supplied to a synthetic imager called Shapeimager (Hasselmann et al. 2021), a Python package that provides 2D synthetic image arrays of small solar system bodies. The images are resolved by projecting the shape model onto the instrument frame at the spacecraft distance and rotational state, thus reproducing the conditions in which the original image was taken. Body latitude and longitude, normal vectors, and incidence, emission, and phase angles are then recovered for each pixel on the visible body cross section. Shapeimager also computes visible, shadowed, and occluded cross sections and all surface-element-based observation angles in reference to the observer, either Earth or LICIAcube, and solar position at the given acquisition time stamp or time range.

3. Disk-integrated Albedo Phase Curve

3.1. Mathematical Definitions

The reduced magnitude $m_{\Lambda(1,1,\alpha)}$ and the flux $F_{\Lambda(1,1,\alpha)}$ are related through the following formula converting the magnitude system to physical radiant flux for a given observer at distance Δ and a light source at distance d (Pravec & Harris 2007):

$$(m_{\Lambda(1,1,\alpha)} - M_{\odot}) = -2.5 \cdot \log\left(\frac{F_{\Lambda(1,1,\alpha)}}{J_{\Lambda 0}}\right), \quad (3)$$

where M_{\odot} is the apparent solar magnitude at $d = 1$ au for some photometric band Λ and $J_{\Lambda 0}$ is the solar irradiance at the target distance for the same given band. We estimate $M_{\odot} = -27.15$ and $J_{R0} = 1.6038 \text{ W m}^{-2} \text{ nm}^{-1}$ for Cousins R, while M_{\odot} and $J_{\Lambda 0}$ LUKE bands are displayed in Table 3. The total flux, integrated through every j th DTM surface element, relates to the radiance factor L_{Λ} for the same surface elements through the equation

$$\sum_j F_{j\Lambda(d,\Delta,\alpha)} = \frac{J_{\Lambda 0}}{\pi d^2} \sum_j \frac{L_{j\Lambda} \cdot \delta S_j}{\Delta_j^2}, \quad (4)$$

where δS is the j th element of a surface cross section in km² at a specific distance to the observer Δ . Given that Didymos's and Dimorphos's DTMs are now known with high precision (Daly et al. 2023), as are their orbital and rotational states at any recent time, the apparent albedo $p_{\Lambda(\alpha)}$ is estimated by assuming that the dependence with phase angle α can be decomposed from topographic brightness, the so-called disk function $D_{(i,e,\varphi)}$

at the DTM surface element j (Shkuratov et al. 2011):

$$\sum_j \frac{L_{j\Lambda} \cdot \delta S_j}{\Delta_j^2} = p_{\Lambda(\alpha)} \cdot \sum_j D_{j(i,e,\varphi)} \Gamma_j \frac{\delta S_j}{\Delta_j^2}, \quad (5)$$

where the radiance factor $L_{j\Lambda}$ is the expression of an active j th DTM surface element reflecting like a homogeneous albedo multiplied by topographic-brightness effects into some photometric bandpass Λ . Then, both sides are integrated into the full body's cross section. Γ is a binary function describing whether the surface is illuminated/visible or not, accounting for all topographic intershadowing and occlusion. As the α increases, the asteroid terminal and nightside become increasingly visible, shadows grow larger, and topographic features occlude one another. We estimate the brightness-topographic function using the so-called Lommel–Seeliger single-scattering law (Fairbairn 2005):

$$D_{ls} = \frac{2 \cos(i)}{\cos(i) + \cos(e)}. \quad (6)$$

The angles i , e , and φ are, respectively, incidence $[0^\circ, 90^\circ]$, emergence $[0^\circ, 90^\circ]$, and azimuth $[0^\circ, 180^\circ]$ (Shkuratov et al. 2011). The total integrated topographic brightness plus illumination, or illuminated disk function, arising from the binary system is therefore given as

$$D_{\text{ill}}^{\text{didy+dim}} = \sum_h D_h \delta S_h \Gamma_h / \Delta_h^2 + \sum_k D_k \delta S_k \Gamma_k / \Delta_k^2. \quad (7)$$

The index h and k represent the h th and k th surface elements associated with each of the bodies' DTMs. We sum over each h th element of Didymos and each k th element of Dimorphos in order to obtain the full cross section. Assuming both having similar reflective properties, to remove Dimorphos's brightness contribution and obtain only the average apparent albedo $p_{\Lambda(\alpha)}^{\text{didy}}$ associated with Didymos, we substitute Equation (5) into Equation (4) and expand the disk function to represent two bodies rather than only one (Equation (7)). At this point, the equation is reordered to place $p_{\Lambda(\alpha)}$ in evidence. The key point is to now consider the total integrated flux $\sum_h F_{h\Lambda(\alpha)} + \sum_k F_{k\Lambda(\alpha)}$ we get from ground-based reduced magnitudes as \bar{F} , the total average flux arising from a binary system of similar reflective behavior. But since we only focus on Didymos's brightness, we multiply $p_{\Lambda(\alpha)}$ by a ratio that balances the primary's scattering cross section to the scattering cross section of both bodies:

$$\bar{p}_{\Lambda(\alpha)}^{\text{didy}} = \left(\frac{\sum_h D_h \delta S_h \Gamma_h}{\Delta_h^2 D_{\text{ill}}^{\text{didy+dim}}} \right) \cdot \left(\frac{\pi d^2 \bar{F}_{\Lambda(1,1,\alpha)}}{J_{\Lambda 0} D_{\text{ill}}^{\text{didy+dim}}} \right), \quad (8)$$

The equation now represents the albedo phase curve of Didymos only, assuming that Dimorphos shares similar reflective properties.

3.2. Ground-based Reduced Magnitudes to Apparent Albedo

Regarding the ground-based observations, a single reduced magnitude represents the integrated signal for the whole observation night for the entire binary system. Thus, in order to obtain the apparent albedo, we integrated the illuminated disk function contribution and cross section for all the night

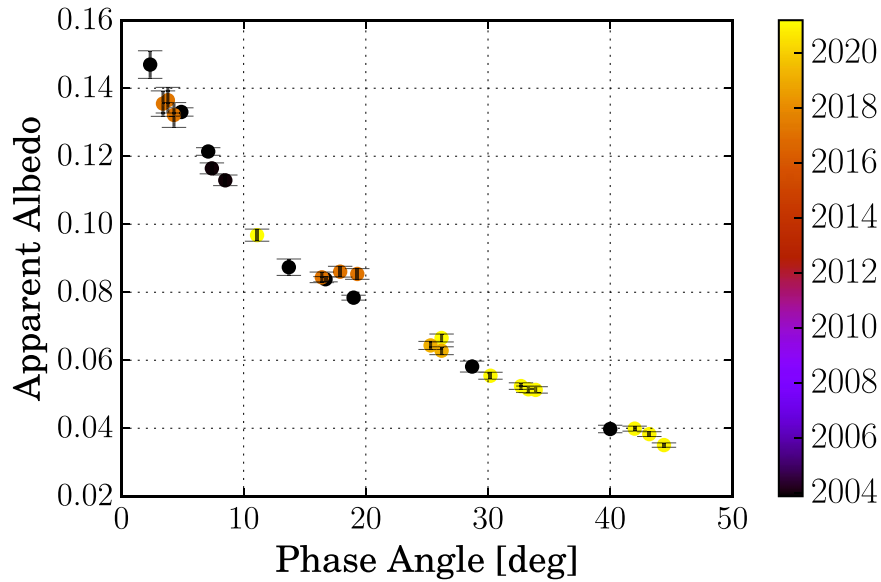


Figure 3. Disk-integrated apparent albedo phase curve of Didymos from the ground-based observations. Color code: yearwise epoch in which the measurement was obtained.

periods for both objects. The Shapeimager was applied for every observation date in Table 1 at a rate of a simulated cross section every $\Delta t = 1h$. The coefficients $D_{ill,t+\Delta t}$ were then integrated for every observation night, taking into account the observability for every station. The results is the apparent albedo p_R for Didymos in function of the phase angle α , as shown in Figure 3. Overall, the albedos are well aligned, with the VLT 2017 observations obtained displaying an overabundance of 7% with respect to 2003’s neighboring observation at 19° – 20° phase angle. As discussed in Section 2.1, that is due to the broad phase angle coverage reported for this specific observational run.

3.3. Apparent Albedo and Magnitude from LUKE Images

The short-exposure LUKE images show the asteroid surface in photometric instrument linearity. Scattered hot or saturated pixels are masked out. The images are recentered with respect to the center-of-figure of Didymos, measured from the synthetic images using Didymos’s projected perimeter. For each image, the total radiance \bar{L}_R was integrated under a photometry circular aperture of a projected radius of 500 m at Didymos’s distance at the center of the image.

By exploiting the images and constraining the plume spatial orientation, we know that most of the ejected material stretches between Didymos and Dimorphos but not between Dimorphos and LICIAcube, with respect to LICIAcube’s line of sight (Deshapriya et al. 2023). Thus, in order to study the contaminating emission sky signal from the plume under Didymos’s aperture, we set three annuli of apertures of 0–10 (annulus 1), 10–20 (annulus 2), and 20–30 (annulus 3) pixels from Didymos’s aperture borders. The annuli and the photometry circular aperture are displayed in Figure 4 along with an image obtained 182 s after impact. The radiance of the plume is about 10%–95% of the signal from Didymos’s surface, depending on the distance to Dimorphos and the phase angle. While a study of the plume is out of our scope, we checked the integrated signal under each annulus and their ratios with respect to Didymos’s total signal. Figure 5 shows the annulus ratios as a function of phase angle. Figure 5 (left)

shows a scatter in the ratios varying up to 45%. Comparatively, annulus 1 has on average 15% more signal than the farther annulus 3 across all phase angles. Annulus 1 is slightly brighter due to the pervading contribution of the outskirts of the “glare” emission near the surface than farther away (more about it afterward), while the spread in the annulus ratios at Figure 5 (left) is due to optically faint ejecta structures near the background level. Figure 5 (right) shows that as Didymos’s surface becomes fainter, the background sky signal level increases up to 40% to the total surface signal as the phase angle increases. Annulus 3 displays the largest deviation around a 55° phase angle due to the proximity to the brightest regions of the plume emission. The background signal and the “glare” become visibly more pronounced as well, indicating a forward-scattering behavior when compared to Didymos’s surface. Henceforth, for our study of Didymos’s phase curve, we limited the subtraction of the background sky signal to that computed from annulus 1.

The so-called “glare” is an emission region near the subsolar point and situated on the side toward Dimorphos’s direction that becomes pronounced with respect to the surface as the phase angle increases (Mazzotta Epifani et al. 2023). Due to the proximity to Didymos’s limb, this feature is hard to remove automatically though computer vision techniques such as flux masking or border-containing synthetic image registration (Hasselmann et al. 2016; for an example, see again Figure 4). Thus, in order to minimize the contribution of the “glare,” inside Didymos’s photometric circular aperture, we set seven confidence levels of 2D contours using statistical built-in tools available for the SAOImage DS9 software (Joye 2006). The fifth level approximately defines the 1σ zone, $\sim 68\%$ of the total feature signal for each selected image. This signal is integrated under a zone that is also inside the photometric circular aperture and subtracted from the total asteroid radiance. For images where the glare signal is brighter than the surface, we set the brightest surface radiance value as the lower cutoff. Otherwise, we set the faintest surface radiance as the upper cutoff and removed the third level from the seventh level. An example of the procedure is shown in Figure 6 for two images,

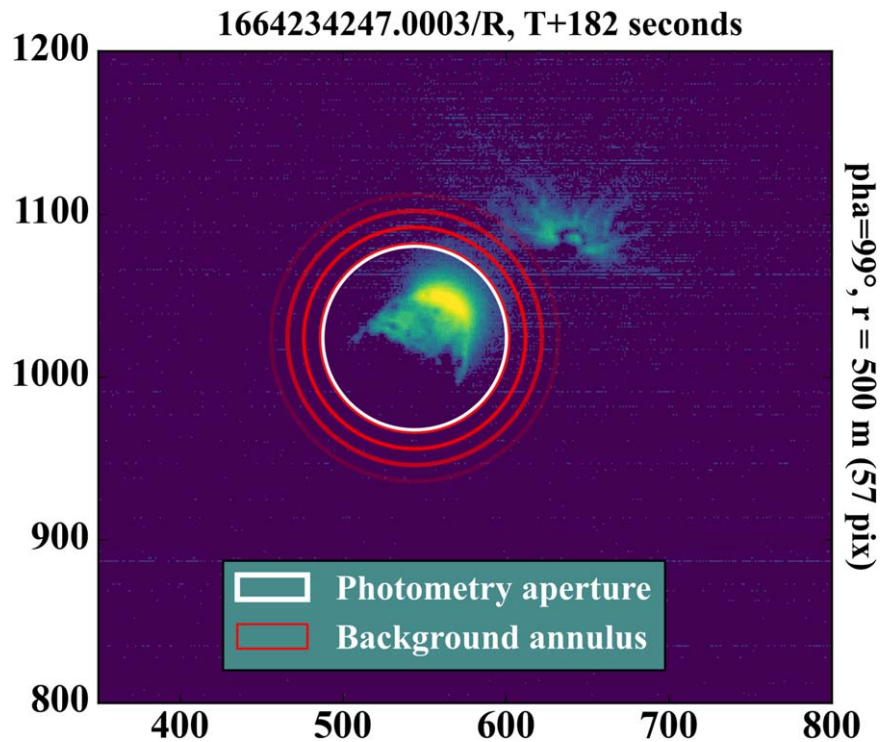


Figure 4. The three annuli under the LUKE/R de-Bayerized image obtained 182 s after the impact (ET 1664234247).

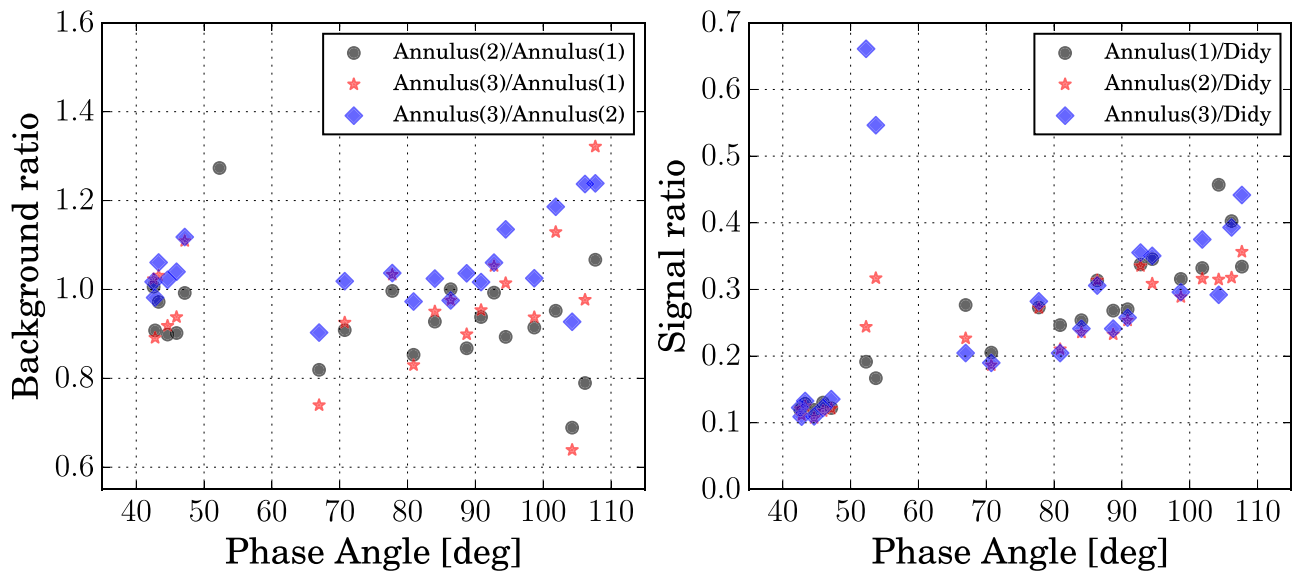


Figure 5. Background analysis with three sky annuli. (Left) Total annulus sky signal ratios. (Right) Total annulus sky signal normalized by the total Didymos signal under the circular aperture.

one before and another after the CA, at 43.3° and 107.7° phase angles.

The final results with the subtracted “glare” emission are shown in Figures 7(a) and (b). The “glare” removal primarily improves the alignment of apparent albedos obtained under a 60° phase angle, before and during the CA, to the data obtained at wider phase angles, after the CA. By the last image in the sequence (ET 1664234259, 107.7° phase angle), the signal is overcome by forward-scattering radiance of the plume contamination and the now $3\times$ stronger signal of the “glare”

emission. This increases the total integrated signal for this specific measurement. Looking into Figure 7(c), overall, the integrated “glare” emission signal contributed as much as the background signal to the total integrated signal. The feature is bright but much more localized. Under LUKE observations, all albedo values cap at a maximum of 0.05 and average of 0.040 ± 0.005 at 43° , connecting smoothly to the ground observation data (0.038 ± 0.002 at the same phase angle; see Figure 3). More on the analysis of the combined data can be found in Section 4.2.

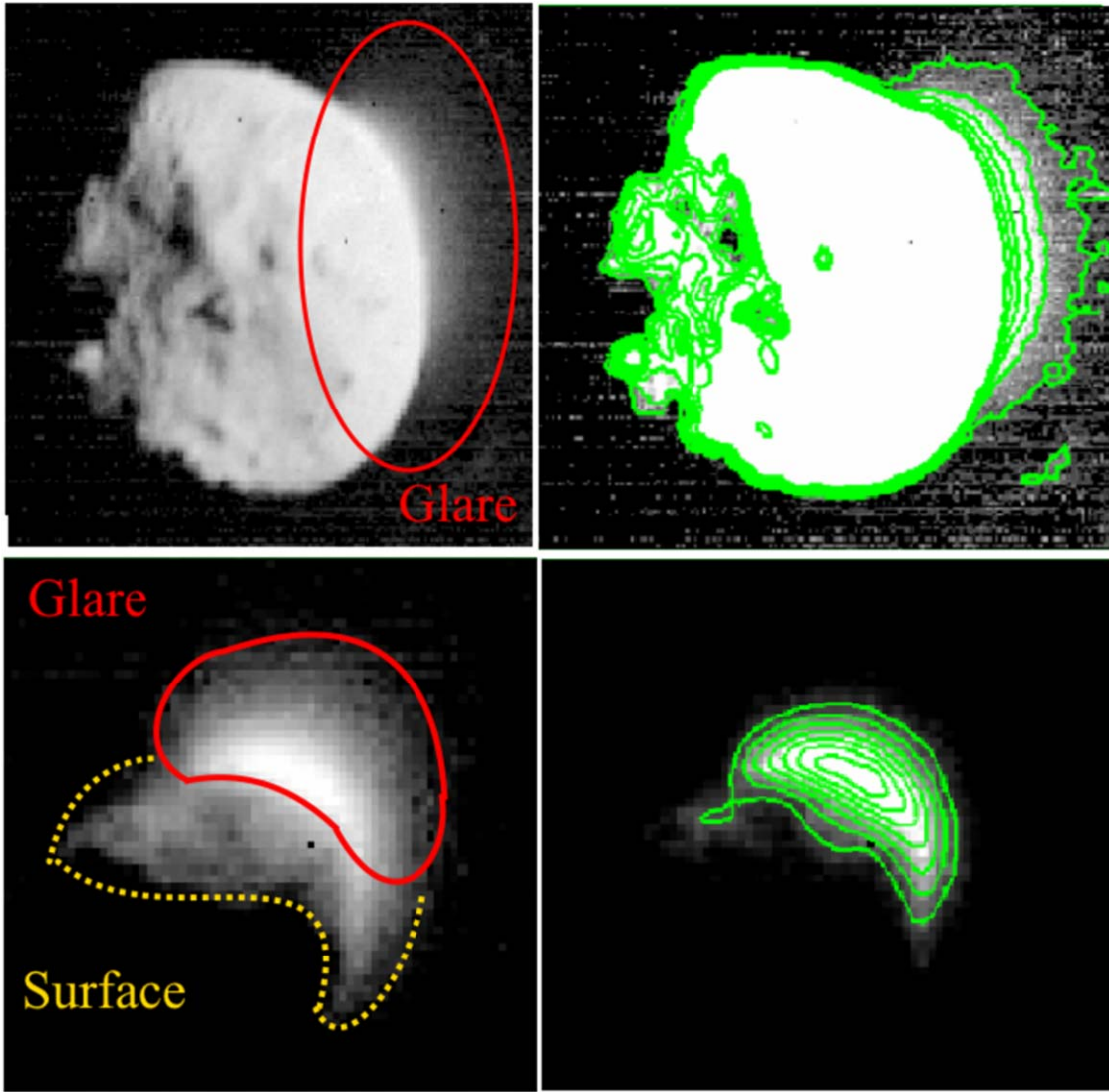


Figure 6. Example of LUKE *R* de-Bayerized images with the “glare” before and after CA under different contrasts. On the left side, the images are stretched using asinh-scale contrast in order to display the asteroid surface and the “glare” together. On the right side, the contrast is scaled linearly and superimposed by the 2D contours. The 2D contours represent seven brightness confidence levels ranging from 0.001% to 99.9% (68% is represented by the fifth level). (Top) Image ET 1664234225, obtained before CA, exposure time of 2 ms, and phase angle of 43.3°. (Bottom) Image ET 1664234259, obtained after CA, exposure time of 3 ms, and phase angle of 107.7°.

4. Results

4.1. Small Phase Angle Analysis: Geometric Albedo and OE

The OE is a phenomenon of nonlinear rise in the surface brightness observed at phase angles smaller than $\sim 5^\circ$ due to intershadow hiding and/or coherent interference effects in granular media. From ground observations of asteroids, this phenomenon becomes broader and more intense as the surface albedo increases, until it reaches a turning point for very high-albedo asteroids (>0.5), such as E types, when the OE peak becomes sharper and less intense (Belskaya & Shevchenko 2000). Since the phenomenon is tightly connected to albedo and asteroid composition, departures from the average OE parameters can indicate unusual surface properties.

We estimated the properties of the OE surge using a set of models that are the most widely used in the last 20 yr and provide a corpus of parametric comparison. These models will be useful to gather a set of parameters in order to compare them with previous solutions published for other asteroids and

provide a set of parameters for future comparison with HERA radiometric data.

(1) The exponential-linear Markov Chain Monte Carlo (MCMC) model,

$$p(\alpha) = a \exp(-\nu\alpha) + k\alpha + b, \quad (9)$$

$$\zeta_{\text{expl}} = 1 + \frac{a}{b}, \quad (10)$$

$$d_{\text{expl}} = \frac{\ln 2}{\nu}, \quad (11)$$

$$\rho_0 = a + b, \quad (12)$$

where a is the exponential amplitude, k is the linear slope coefficient, and b is the y-intercept coefficient. We then derive the OE intensity ζ_{expl} , the OE half-width at half-maximum (HWHM) d_{expl} , and the geometric albedo ρ_0 . The subscript expl corresponds to the parameters associated with the exponential-linear model.

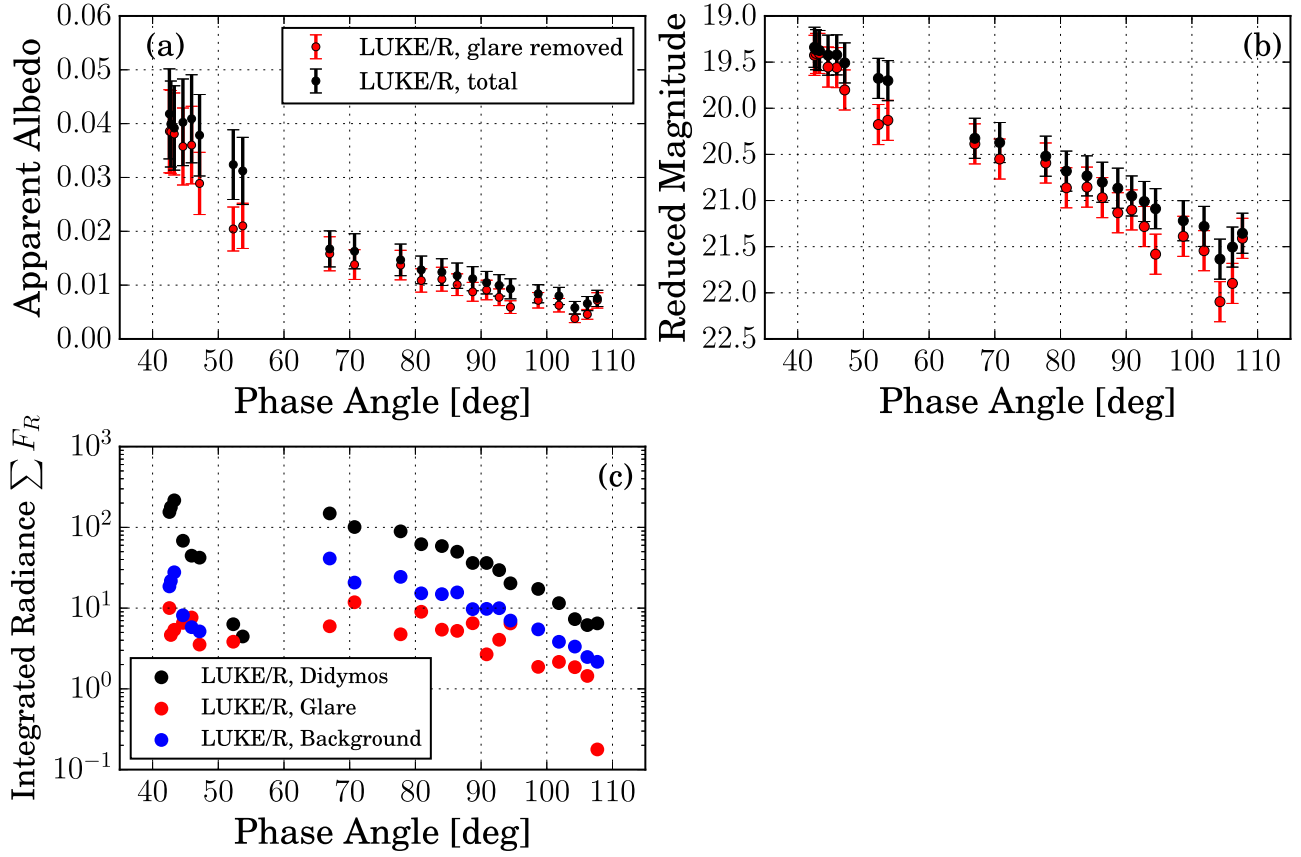


Figure 7. The “glare” emission analysis with respect to Didymos’s signal. (a) Didymos’s LUKE/R apparent albedo and (b) magnitude phase curve before (black) and after (red) subtracting the “glare” emission. (c) The integrated radiance $\sum F_{R(1,1,\alpha)}$ for Didymos, the “glare” emission, and sky background from annulus 1 for every preselected LUKE/R image.

The exponential-linear equation is applied to albedo or radiance phase curves under a 50° phase angle, where the exponential-like trend is more evident. To be consistent with previous applications of this model, the solution was studied through the MCMC approach (Muinonen et al. 2009). The MCMC is the core of Bayesian inference techniques: unknown variables in the model are treated probabilistically, where the techniques’ target is to estimate the posterior probability function (PDF) for each unknown variable. The PDFs will then describe the most probable values for the variable in its own space range and also any correlation with other variables in the model. MCMC starts from prior PDFs representing any a priori knowledge about the variables and then promotes controlled random walks that explore the multivariate space through maximizing the normal log-likelihood function. After a sufficient number of draws, the chain will correspond to the “true” posterior PDF, independently of any a priori knowledge. Posterior PDFs are not necessarily unimodal symmetrical normal-like distributions, and the MCMC approach enables resolving the skewness and multimodality of such distributions, which subsequently leads to a better understanding of the solutions and uncertainties associated with the parameter. The random walks are sampled using the Hamiltonian No U-Turn Sampler (NUTS) algorithm alongside two parallel chains of 11,000 draws in total (Hoffman & Gelman 2014). The exploitation of two chains is the minimum used to check for divergences and convergences in the sampling. The Hamiltonian Monte Carlo uses the local derivatives and dynamics to explore the multivariate space more efficiently.

In Figures 8(a)–(d), we show the correlation among the posterior PDFs. The posteriors therein are described by correlated unimodal distributions, with the central median and median absolute deviation stated in Table 4. The median solution yields a coefficient of determination of $R^2 = 0.992$. The coefficient is equal to 1 minus the ratio between the sum of squared residuals over the total sum of squared deviations to the mean. As it gets closer to unity, a higher percentage of the sample variance is explained by the that model to which the data is compared. The function yields a ζ_{expl} of 1.69 ± 0.05 and a d_{expl} of $6.2^\circ \pm 1.5^\circ$.

(2) The linear-by-parts model,

$$\begin{aligned} p_{2l}(\alpha < 5^\circ) &= -A_0\alpha + B_0 \\ p_{2l}(\alpha > 10^\circ) &= -A_1\alpha + B_1, \end{aligned} \quad (13)$$

$$\zeta_{2l} = \frac{B_0}{B_1}, \quad (14)$$

$$d_{2l} = \frac{(B_0 - B_1)}{2(A_0 - A_1)}, \quad (15)$$

where A_i are the linear slope coefficients and B_i are the y-intercept coefficients. The index $i = 0$ is being associated with $\alpha < 5^\circ$, while $i = 1$ is being associated with $\alpha > 10^\circ$. $2l$ is the subscript linked with the linear-by-parts model.

Linear-by-parts is a simple model first proposed by Lumme & Irvine (1976) to describe the change in steepness between two regimes in the phase curve. The model was retaken by Déau et al. (2009, 2016) and applied to OEs of meteorite

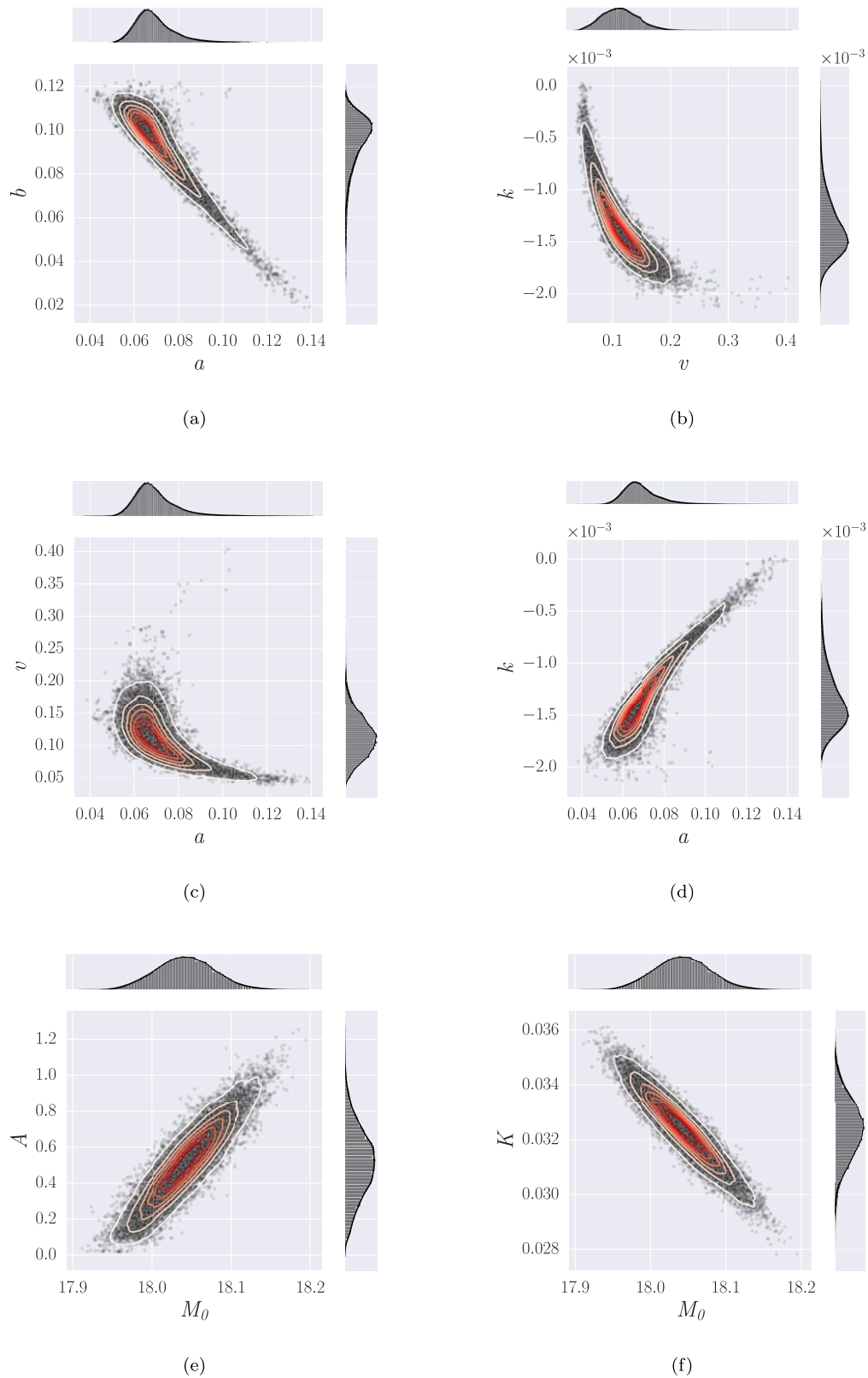


Figure 8. The 2D posterior PDFs for (a), (b), (c), (d) the exponential-linear parameters and (e), (f) the “Shevchenko” function parameters. The dark dots represent the total of 22,000 draws from the MCMC NUTS. The posterior PDFs are superimposed by seven confidence levels in shades of red, in which the 1σ level is comprised of the second contour from inner to outer levels. Alongside the XY -axis, we display the PDFs projected onto a single parametric space and normalized to unity.

samples and outer solar system bodies. For $\alpha < 5^\circ$, the regime is influenced by the nonlinear OE, whereas for $\alpha > 10^\circ$, the phase curve is now mainly controlled by the single-scattering

phase function and surface roughness. We fit both lines using the OLS regression, as similarly done for the ground observations. The best solution and associated uncertainty are

Table 4
Central Solutions for the Ground Observation Phase Curve with Respect to the Three Models

(1)	Exponential-linear (2)	(3)	Linear-by-parts (4)	(5)	“Shevchenko” Function (6)
ρ_0	0.165 ± 0.006	$M_{(1,1,0)}$	17.53 ± 0.03
a	0.068 ± 0.005	B_0	0.162 ± 0.004	M_0	18.04 ± 0.02
b	0.098 ± 0.007	A_0	-0.007 ± 0.001	A	0.5 ± 0.1
v	0.11 ± 0.02	B_1	0.114 ± 0.002	K	0.0324 ± 0.0005
k	-0.0014 ± 0.0002	A_1	$-1.83 \pm 7.6 \cdot 10^{-5}$	COB	0.94 ± 0.1
ζ_{expl}	1.69 ± 0.05	ζ_{2l}	1.42 ± 0.06	ζ_{shev}	0.43 ± 0.08
d_{expl}	$6.2^\circ \pm 1.5^\circ$	d_{2l}	$4.6^\circ \pm 1.8^\circ$	d_{shev}	$2.8^\circ \pm 1.0^\circ$

listed in Table 4. It is worth noting that for $\alpha < 5^\circ$, the opposition regime is described by only five data points; thus, the linear fit yields a subestimation of the geometric albedo with respect to the exponential-linear function but falling under the calculated uncertainties. The model yields an amplitude of the OE ζ_{2l} of 1.42 ± 0.07 and HWHM d_{2l} of $4.6^\circ \pm 1.6^\circ$. The coefficients of determination are $R^2_{(\alpha < 5^\circ)} = 0.932$ and $R^2_{(\alpha > 10^\circ)} = 0.971$, whereas the model performs more poorly for the scant data near zero phase angles.

(3) The three-parameter empirical “Shevchenko” function,

$$m(\alpha) = M_0 - A/(1 + \alpha) + K\alpha, \quad (16)$$

$$\zeta_{\text{shev}} = I(0^\circ 3)/(M_0 + K \cdot 0^\circ 3), \quad (17)$$

$$d_{\text{shev}} = \alpha(\min((A/(1 + \alpha_j) + K\alpha_j)^2)), \quad (18)$$

$$\text{COB} = \zeta_{\text{shev}}/I(0^\circ 3)/I(5^\circ), \quad (19)$$

where M_0 is the linear absolute magnitude, A is the intensity of the nonlinear term, and K is the linear slope coefficient. COB is the estimated percentage of coherent backscattering contribution. $I_{(\alpha)}$ is the flux obtained using the flux-magnitude formula (Equation (3)), and shev is the subscript linked with the “Shevchenko” function.

The “Shevchenko” function (Shevchenko 1996) is applied to magnitude phase curves under 50° phase angle, and, similarly to the linear-exponential function, it describes the nonlinear and linear regimes in the curve. The model is the basis for the derived trends for asteroids presented in Belskaya & Shevchenko (2000), which provided relationships between asteroid spectral types and OE parameters. We studied the solutions using the MCMC approach as well, using the same sampler and number of draws as for the exponential-linear function. The median solution and associated uncertainty are listed in Table 4. The posterior PDFs are displayed in Figures 8(e) and (f). The magnitude phase curve is linear down to the very small angles, pushing the amplitude A to be very small as well. The linear slope K is consistent with the coefficient derived from a linear fit only (Section 2.2). The median solution yields the highest coefficient of determination of $R^2 = 0.993$. This coefficient is higher than fitting a simple line (Section 2.2; $R^2 = 0.990$), indicating a small improvement over the small phase angles. The OE amplitude ζ_{shev} is 0.43 ± 0.08 , and the HWHM d_{shev} is $2.8^\circ \pm 1.0^\circ$. The Shevchenko function yields the smallest HWHM and the best adjustment among the models.

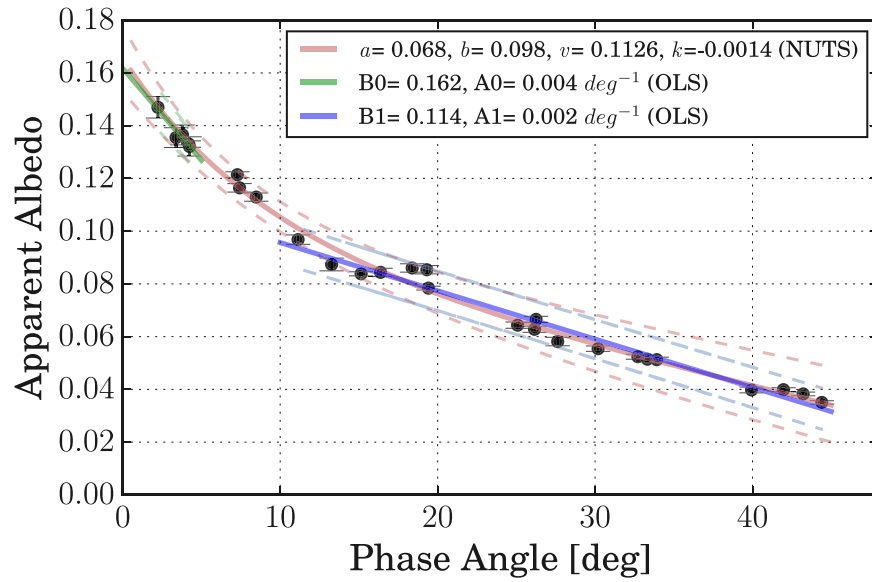
Finally, the data points alongside the central solutions for each model are shown in Figure 9. In Figure 9(a), the linear-by-parts OLS solution and exponential-linear NUTS median solution are confronted with the apparent albedo phase curve, while in Figure 9(b), the NUTS median solution from the

“Shevchenko” function is then confronted with the magnitude phase curve. The envelope represents the associated 1σ uncertainties to the solution.

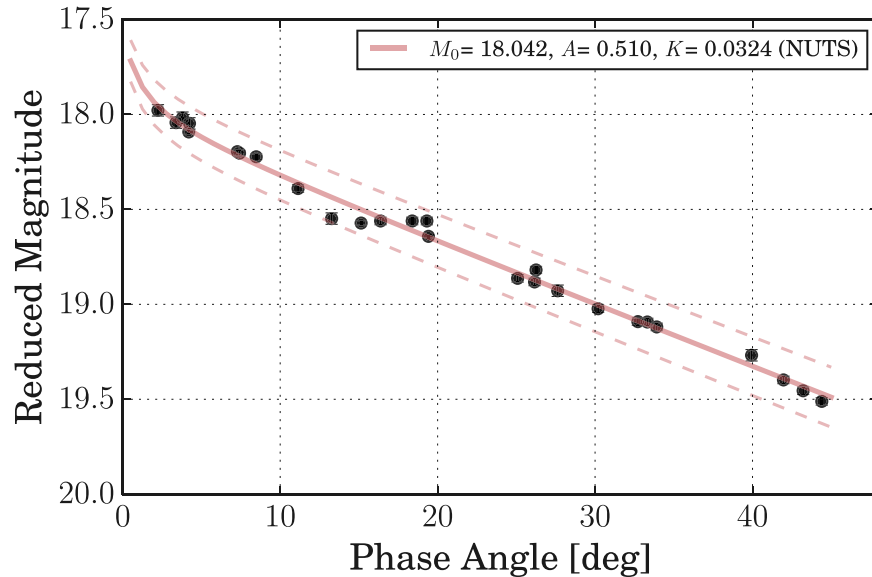
In the next step of the analysis, we compared the derived parameters to empirical trends from Belskaya & Shevchenko (2000), Kaasalainen et al. (2003), and Déau et al. (2016) (hereafter BS2000, BS2000, K2003, and D2016, respectively). Provided the most comprehensive asteroid OE trends in the literature. They computed the linear phase slope and OE parameters for 33 large main-belt asteroids with exceptional phase angle coverage from diverse spectral types. We thus place Didymos OE parameters computed using the “Shevchenko” function into Figure 10. The Figure 10 plots were reproduced from BS2000 accordingly using recovered data for the 33 asteroids therein. The parameters fall well among the M types, near the outer boundary of the S-type clusters toward C types. We point out that Didymos’s geometric albedo is darker and the linear phase slope steeper than what is found for large main-belt S-type asteroids. Intensity ratio $I(0.3^\circ)/I(5^\circ)$, ζ_{shev} , and d_{shev} indicate a larger OE amplitude and narrower OE width than the large silicate main-belt asteroid in the sample.

By characterizing the OE under the linear-exponential model, asteroid parameters from diverse spectral types were studied by K2003. Like BS2000, K2003 gathered a subset of large main-belt asteroids with broad phase angle coverage. Their sample covers mostly S and M types, for which their PDFs were provided in ζ_{expl} and d_{expl} space (called $(a + b)/b$ and d therein). In Figure 11(a), Didymos’s partial solution space is superimposed into the K2003 S-type parameter space, adapted and reproduced from their Figures 7, 8, and 14. Even considering the large uncertainties associated with this modeling, Didymos’s exponential-linear OE is equally found outside the expected S-type region. Looking further into the list of studied asteroids from K2003, it indicates that Didymos situates nearer G and C types instead (Ceres, $\zeta_{\text{expl}} = 1.47$ and $d_{\text{expl}} = 3.70^\circ$; and (24) Themis, $\zeta_{\text{expl}} = 1.37$ and $d_{\text{expl}} = 3.50^\circ$) but much broader and more intense in terms of this model. We overplotted in Figure 11(a) the PDFs associated with the solution for both asteroids. Ceres is well situated midway between C and M types in the BS2000 trends as well (see again Figure 10; Ceres is the only G-type object in the plot).

The linear-by-parts model allows for comparing Didymos to meteorites studied by Déau et al. (2016). We thus present in Figure 11(b) Didymos’s ζ_{2l} (called A therein) and B_0 (called albedo therein) superimposed into the meteorite trend. Figure 11(b) is adapted and reproduced directly from Figure 7 and Table A1 in Déau et al. (2016). We refer the reader to the original article for more details about the samples. This kind of comparison has to be done carefully, since the meteoritic sample preparation does not generally represent the natural



(a)



(b)

Figure 9. Smaller phase angle observation of Didymos from ground-based observations and fitting models. (a) Linear-exponential (light red) and linear-by-parts (light green and blue). (b) The “Shevchenko” function (light red). The associated envelope of the same color (dotted line) represents 1σ uncertainties.

microphysical state in which the asteroid soil is found. It is worth noticing that Déau et al.’s (2016) powdered samples were all prepared with grain sizes under $100\ \mu\text{m}$ radius. For ordinary chondrites, this indicates geometric albedos 10% higher than for sizes $>500\ \mu\text{m}$ (Bowen et al. 2023), an offset that apparently does not change Figure 11(b) in broad terms. In addition, Beck et al. (2012) show that the OE amplitude in meteorites also trends with geometric albedo as well, a similar scenario found among asteroids. We find Didymos situated among L chondrites in the diagram rather than LL chondrites. LL ordinary chondrites, Didymos’s meteoritic analog according to VIR-NIR spectral data (de León et al. 2010; Ieva et al. 2022b), is represented by only two samples (Olivenza, St Mesmin/St Severin) in the diagram, with albedos well over 0.2. It is also worth noting that among the L chondrites,

Didymos is situated very close to the Mezö-Madaras meteorite. Mezö-Madaras is a brecciated, volatile- and carbon-bearing, primitive unequilibrated L3.7 ordinary chondrite (Van Schmus 1967; Mostefaoui et al. 1995). This comparison alone sets an alternative hypothesis for the darkening material, which is further discussed in Section 5.

4.2. Full Phase Curve Analysis: Curve Morphology and HG/HG1G2 Parameterization

The full Didymos magnitude curve from 2.35° to 107.7° of phase angle is remarkably linear, with no obvious features associated with the OE or the topographic shadowing roughness. The first assessment of the curve morphology was done by Kitazato et al. (2004) using four magnitude points for fitting the IAU-legacy HG magnitude system (Bowell et al. 1989).

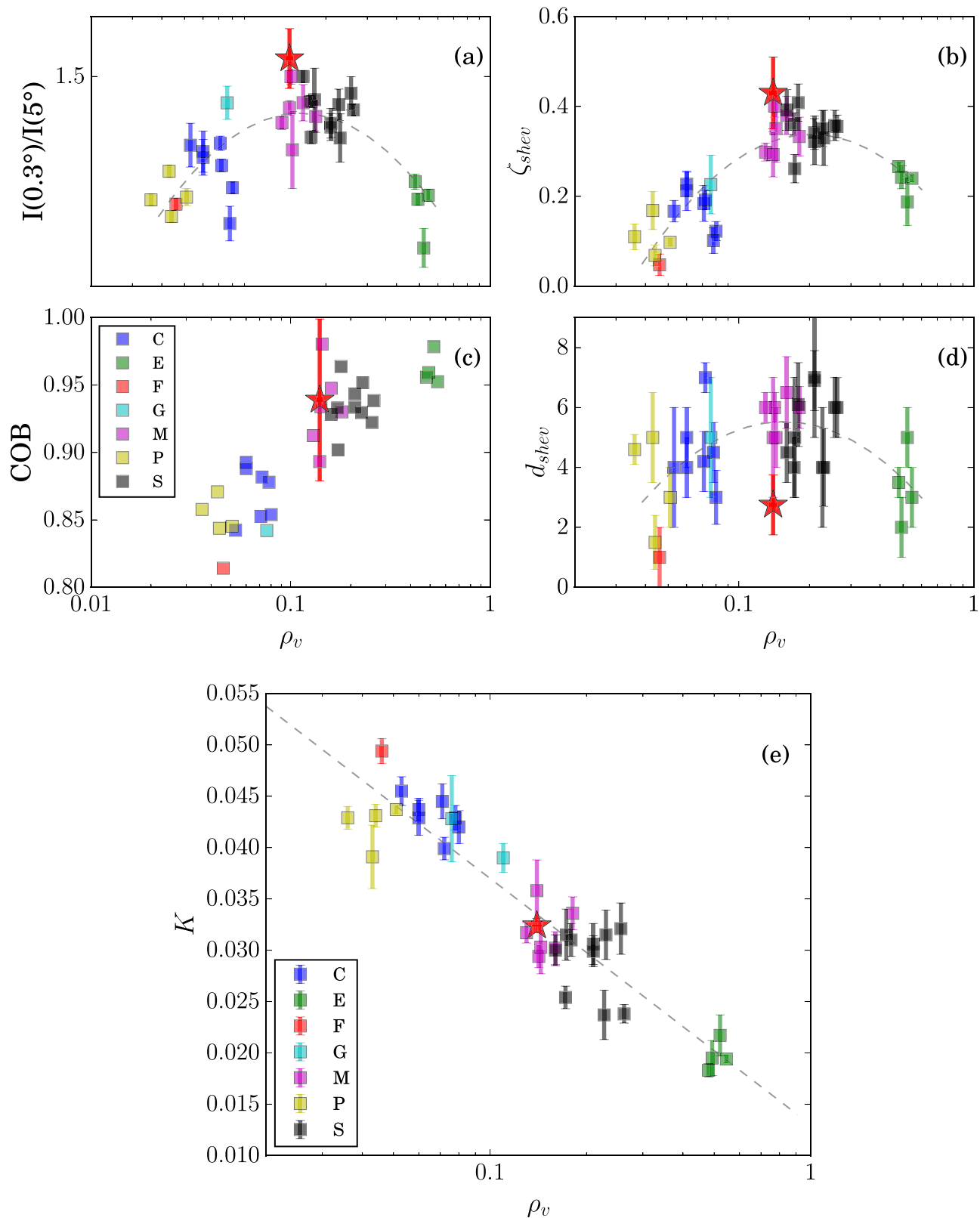


Figure 10. Didymos’s “Shevchenko” parameters compared to ground-based observations of asteroids from data shared by Belskaya & Shevchenko (2000). The asteroid data are classified and color-coded by spectral type. Didymos’s R Cousins albedo is translated to Johnson V ρ_v using $(V-R)$ color reported by Kitazato et al. (2004). Didymos is represented by a red star. (a) Intensity ratio $I(0.3^\circ)/I(5^\circ)$, (b) OE intensity ζ_{shev} , (c) COB, (d) OE HWHM d_{shev} , (e) linear phase slope coefficient K as function of ρ_v . The traced lines in (a), (b), and (d) represent the spline fit calculated by Belskaya & Shevchenko (2000). In (e), the dashed line represents the log-linear fit shown in Belskaya & Shevchenko (2000, their Figure 4). Errors are represented by error bars or the symbol size; the largest prevails.

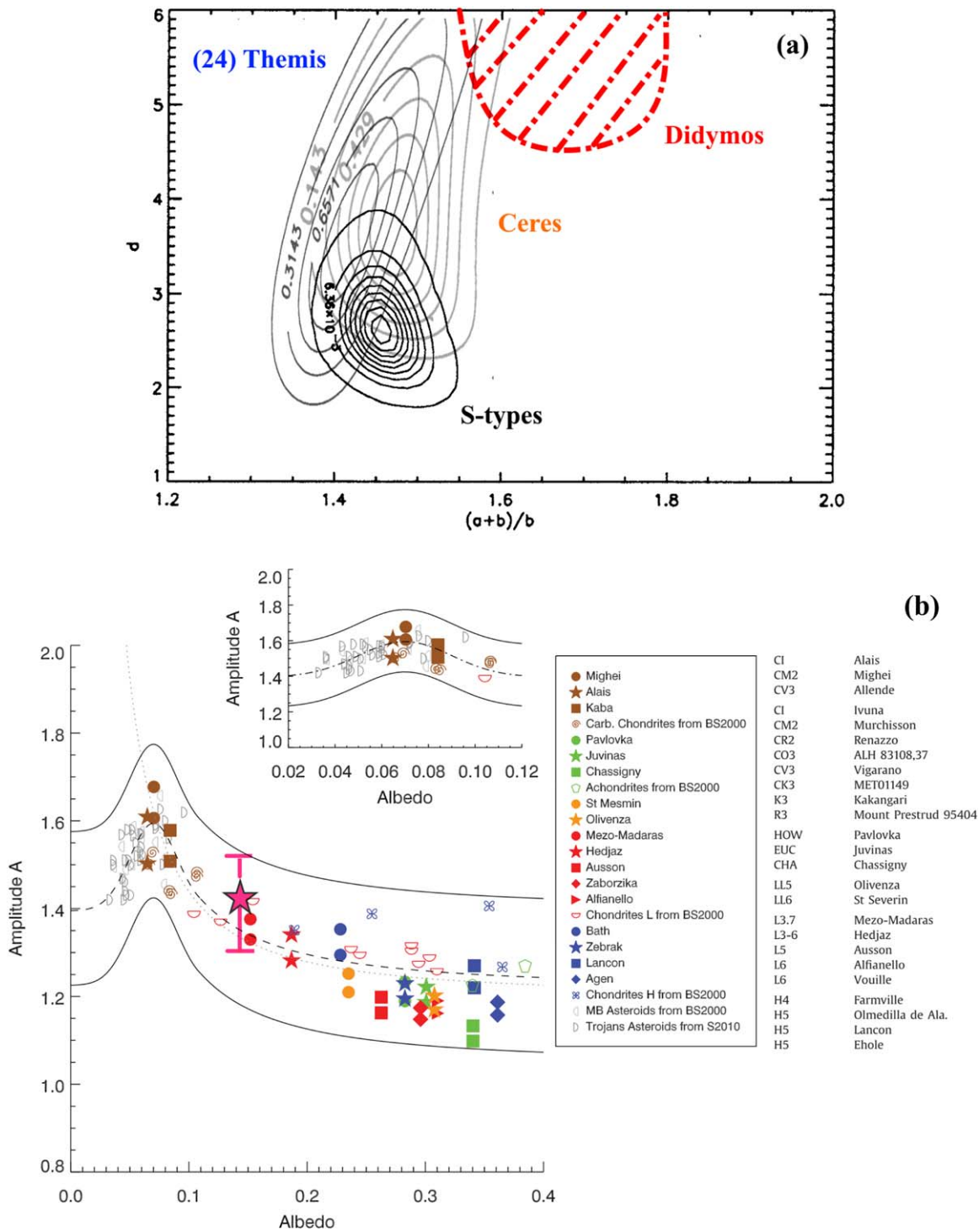


Figure 11. Didymos’s exponential-linear and linear-by-parts parameters compared to asteroids and meteorites. Didymos’s R Cousins albedo is translated to Johnson V using the $(V-R)$ color reported by Kitazato et al. (2004). (a) Parametric PDF in exponential-linear OE intensity ζ_{expl} and HWHM d_{expl} ($(a+b)/b$ and d therein, respectively) space S types, (24) Themis, and Ceres adapted and reproduced by overplotting Figures 7, 8, and 14 from Kaasalainen et al. (2003). Didymos’s parametric region is contained under the dashed-dotted red zone and partially off the boundaries defined by the original figure. (b) Linear-by-parts OE intensity ζ_2 and albedo B_0 (amplitude A and albedo therein, respectively) of meteoritic data adapted and reproduced from Figure 7 and Table A1 in Déau et al. (2016). Déau et al.’s (2016) powdered samples (radius $< 100 \mu\text{m}$) are selected from the RELAB database. Didymos is represented by a magenta star. Errors are represented by error bars or the symbol size; the largest prevails.

HG is an empirical function developed to describe the morphology of asteroid magnitude phase curves. Kitazato et al. yields $H_R = 17.70$ and $G = 0.20$, parameters that place Didymos among ordinary S types. Our reassessment with a larger phase coverage using the Pyedra package (Colazo et al.

2022), however, yields a weaker G parameter, $G = 0.129 \pm 0.01$, again situating Didymos ambiguously between S and C complexes ($G_S = 0.25 \pm 0.06$ and $G_C = 0.15 \pm 0.09$, respectively; Vereš et al. 2015). Overall, the HG system fits the phase curve well, describing the nonlinearity of points at $\alpha > 80^\circ$,

generally associated with shadowing macroscopic roughness on the surface. A simple linear fit (OLS regression; see Section 2.1) in absolute magnitude yields a phase slope coefficient ($H_R = 17.91 \pm 0.02$ and slope = 0.032 ± 0.004) very similar to ground observation only, reinforcing the unusual linear and steeper Didymos phase curve.

We further studied the full phase curve morphology using the IAU official HG1G2 magnitude system (Muinonen et al. 2010). H is the absolute magnitude, and G1 and G2 are the morphological parameters in the reduced magnitude phase curve. The parameters are arranged through the formula

$$m_{\Lambda}(1, 1, \alpha) = H - 2.5 \cdot \log(G1\Phi_1(\alpha) + G2\Phi_2(\alpha) + (1 - G1 - G2)\Phi_3(\alpha)), \quad (20)$$

where Φ_1 and Φ_2 are functions controlling the curve shape at mid- and wider phase angles, while Φ_3 defines the morphology in the OE regime ($\lesssim 7.5^\circ$). In Figure 12, we show the parameterizations above alongside the apparent albedo and magnitude points. The linear parameterization fits the data at smaller phase angles ($< 5^\circ$) poorly, while HG and HG1G2 functions underperform for nonlinear features at wider phase angles ($> 80^\circ$).

The latest homogeneous corpus for a large asteroid sample was recently provided by Mahlke et al. (2021). Based on the dual-band photometry (cyan: 410–660 nm; orange: 560–810 nm broad bands) acquired by the Asteroid Terrestrial-impact Last Alert System (ATLAS) telescopes, Mahlke et al. studied 127,012 phase curves of 94,777 asteroids, derived their HG1G2 parameters, and checked for relations with spectral types and asteroid families. We focus on comparing to the cyan observations only, since magnitudes in this filter present smaller uncertainties. Didymos's HG1G2 parameter is obtained using the online tool available from the Planetary System Research group at the Department of Physics, University of Helsinki (Penttilä et al. 2016).²¹ Didymos's parameters are $H_R = 17.74 \pm 0.14$, $G1 = 0.73 \pm 0.13$, $G2 = 0.17 \pm 0.03$, $\rho_{0,R} = 0.16 \pm 0.01$, and a coefficient of determination $R^2 = 0.980$.

In Figures 13(a) and (b), Didymos's HG1G2 parameters are compared with the central parameters for S, M, C, and D types. Under a 40° phase angle, Didymos might well be misinterpreted as C or D type, if only this phase curve regime had been sampled, while, when including data for 40° or higher, it posits Didymos among D types. It is important to notice that Didymos does not display the same sharpness or narrowness in the OE regime as seen for brighter asteroids as well as for S types. Its OE inflection around 5° is not visually remarkable. The ambiguities are broken with the addition of LUKE data for wider phase angles. Phase-curve-wise, G1-G2 parameters as well as morphology place Didymos under the 1σ PDF space of the C-type asteroids. Looking into the macrogroup of spectral types associated with carbon-based compositions, the C-type G1-G2 center is near the P, B, and Ch types (Mahlke et al. 2021). Also, interestingly, a C-type PDF is sufficiently broad to cover part of the S-type space (C-type region for PDF $> 45\%$), indicating a pervading ambiguity of asteroids classified as C types to S types, according to G1-G2 analysis only. S-type asteroids are otherwise more rarely misclassified as C types, furthering the unusual “situation” in which Didymos is found.

4.3. Comparison with Phase Curve Parameters of NEAs

Didymos, being part of the small NEA population, is subjected to the internal and external processes that change their surfaces differently than larger asteroids in the main belt. YORP, impacts, thermal erosion, electrostatic lofting, and close planetary encounters can shake off the surface from certain grain size ranges and/or mix less-weathered underground layers with the older and exposed upper layers. These processes will not only modify the asteroidal spectral properties but are also expected to change the phase curve morphology. However, for every body, these resurfacing processes can be incomplete or more or less efficient depending on their mineralogy, diameters, shape, and grain/boulder size frequency distribution. Hsu et al. (2022) shows that, when balancing all the aforementioned resurfacing processes, small asteroids (less than roughly 1 km in size) are depleted by half of their fine submicrometric grains in 1.2 Myr, while large asteroids (larger than 10 km in size) are able to preserve this grain fraction and get their surface dominated by it during their lifetime.

Whereas most of the trends observed in phase curve parameters are drawn from samples of larger main-belt asteroids, Ieva et al. (2022a) indicate that NEAs display more diverse OE and curve morphology from a sample of 15 asteroids. They populate the outskirts of the spectral-type core clusterings in those trends, alluding to a broadening of the albedos' and parameters' variance in place. Arcoverde et al. (2023) studied a small sample of NEAs as well. They estimated the G1-G2 parameters of 12 NEAs and noted no correlation between geometric albedo and their position in the G1,G2 space. Now, knowing that Didymos also displays unusual behavior for an S type when placed in those same trends, we seek to compare it with those asteroids of the same size range and dynamical population.

First, it is worth noticing that the study of phase curves for NEAs remains very limited. In addition to the two previously cited studies, we scraped the NASA/JPL database²² and the literature (Lederer et al. 2008; Ishiguro et al. 2014; Reddy et al. 2015; Hergenrother et al. 2019; Huang et al. 2021) looking for small $\lesssim 2$ km NEAs. We gathered a total of 25 small NEAs, where 18 have reported rotational periods higher than 2.5 hr. In Table 5, we list the parameters from the literature and JPL database for the objects selected for comparison.

In Figure 14, Didymos is superimposed onto diagrams comparing it to the OE amplitude z_{shev} , phase slope coefficient k , geometric albedo ρ_v , and rotational period, as well as the G1-G2 parameters for the NEAs listed in Table 5. A noticeable behavior among NEA S types is that their locus is offset to more intense OE amplitudes than the main-belt S types, with many objects sitting very close to Didymos. In the G1-G2 space, the NEA S types are situated in the outskirts of the central core of main-belt S types as well. One NEA S type in particular, 2005 TF, has very similar ρ_v ($=0.154 \pm 0.040$), rotational period ($=2.7$ hr), and diameter ($=0.59 \pm 0.20$) to Didymos but much stronger z_{shev} and less steep k . Didymos has the shortest rotational period ($=2.26$ hr) in the sample, very similar to Apollo (Q type), 2002 LJ3 (Q type), 2004 BL86 (V type), and the aforementioned 2005 TF (S type). Apollo, to which, interestingly, Didymos's k and G1-G2 are also situated very close to (1862) Apollo in the diagrams.

²¹ See <https://psr.it.helsinki.fi/HG1G2/> (2023 November).

²² See <https://ssd.jpl.nasa.gov/tools/> (2023 November).

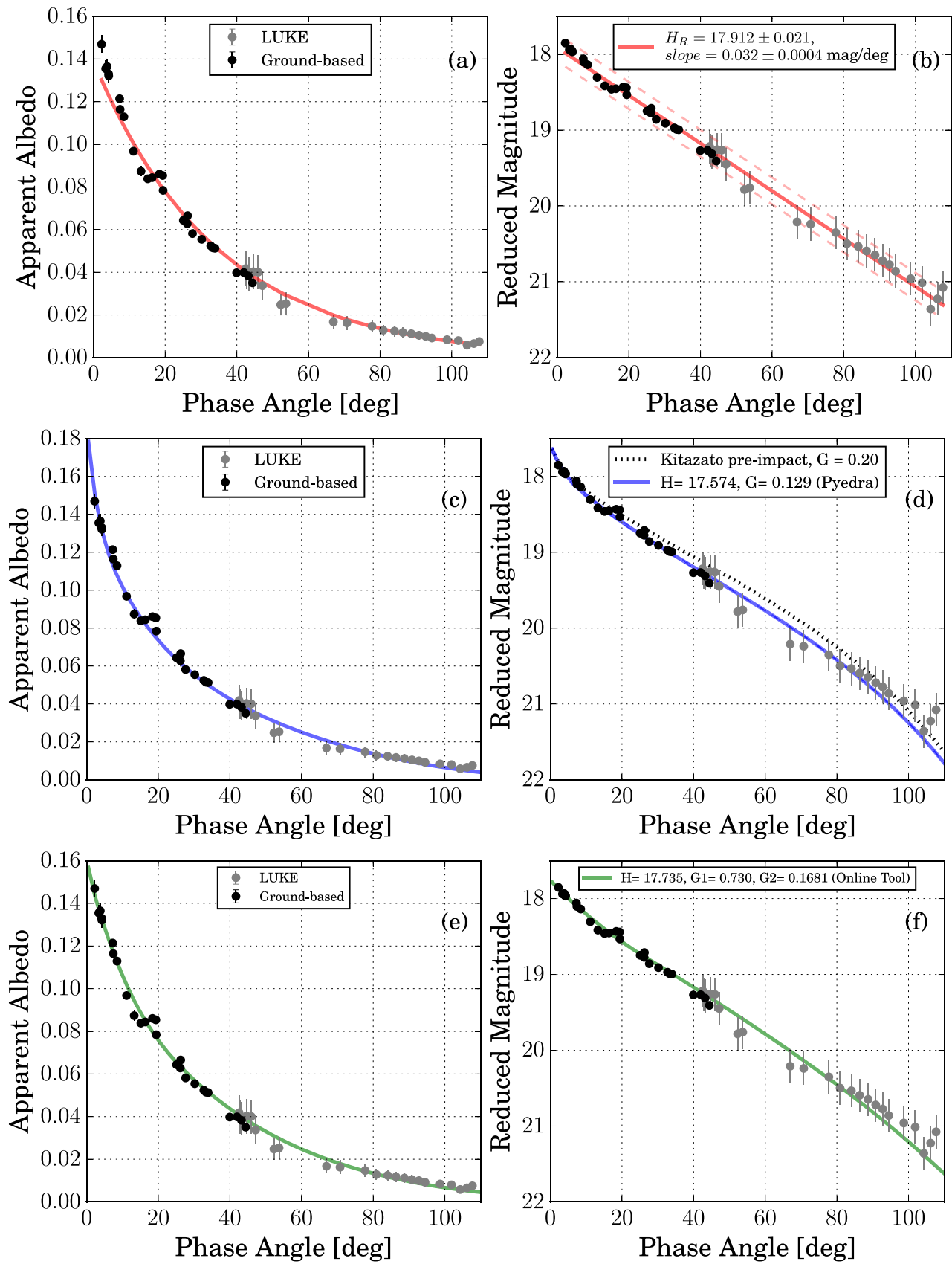


Figure 12. The full brightness phase curve of Didymos in Cousins *R* using LUKE/RGB and ground-based observations. Apparent albedo derived from the equations in Section 3.1. Data are confronted with the ((a), (b)) linear, ((c), (d)) HG, and ((e), (f)) HG1G2 curves from solutions in Table 4. Panel (f) is displayed alongside Kitazato et al.'s HG solution.

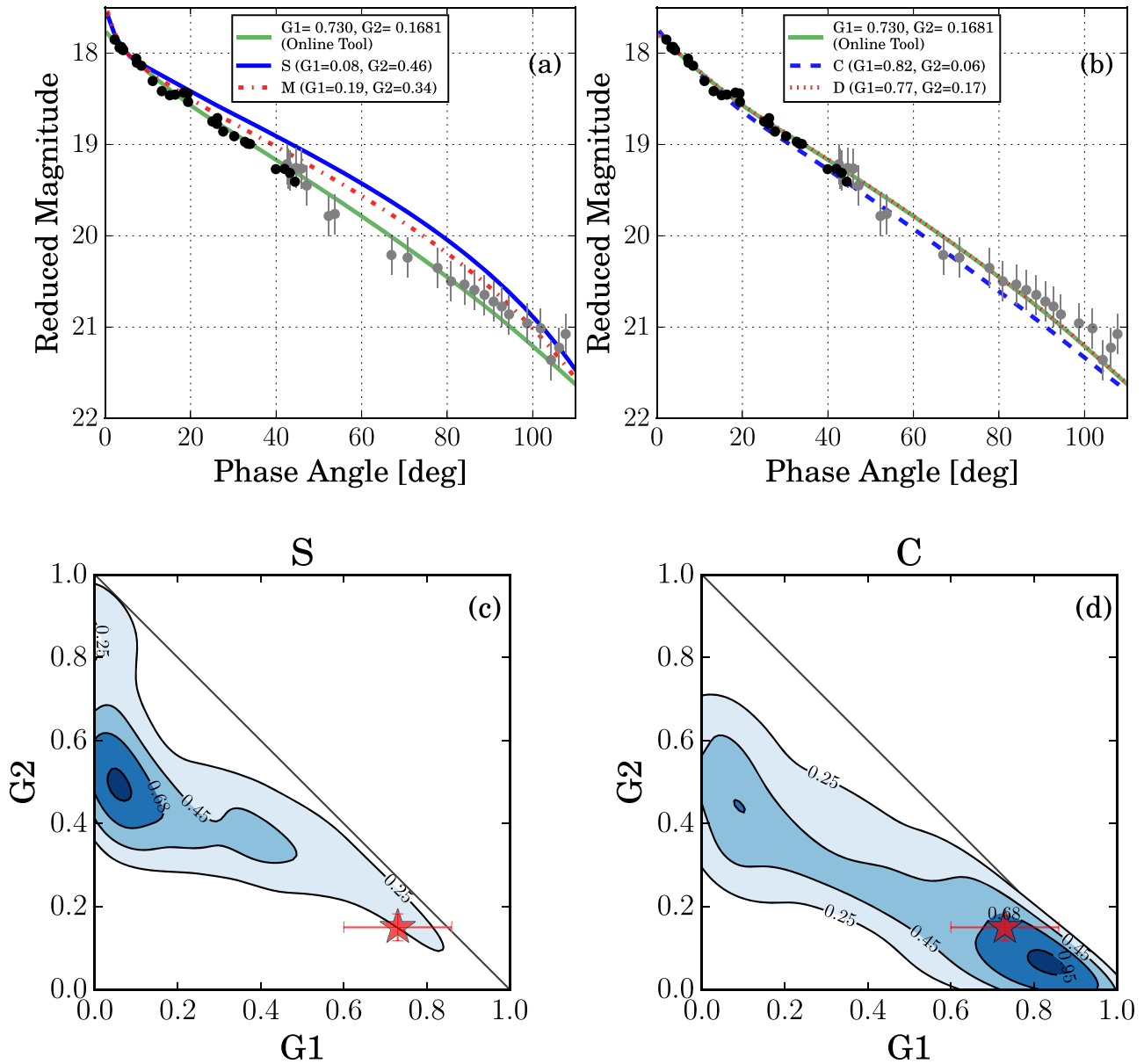


Figure 13. Didymos’s HG1G2 phase curve compared to other asteroid spectral types. (a) and (b) Central HG1G2 parameters for asteroid spectral types obtained from Mahlke et al. (2021). The absolute magnitudes for all the phase curves associated with the spectral types were set to the same Didymos m_R magnitude at a phase angle of 5° for better comparison. (c) Diagram of G1-G2 2D PDF for S types observed by ATLAS in the cyan band. This diagram is a reproduction of similar diagrams presented by Mahlke et al. (2021). Didymos’s G1-G2 is represented by a red star. The colored levels represent the probability associated with regions in the distribution. (d) Similar to (c) but for the C-type asteroids.

(1862) Apollo is the name-giver to a dynamical group of Earth-crossers of low eccentricity and semimajor axis of which Didymos is a part. The asteroid Apollo is a Q type, a lower-spectral-slope taxonomic class of asteroids more akin to ordinary chondrites due to the surface refreshing through induced resurfacing by close planetary encounters (Nesvorný et al. 2005; Binzel et al. 2010; DeMeo et al. 2023). Apollo and Didymos are both potentially hazardous asteroids, with MOID under 0.05, and both are also orbited by a secondary body (Ostro et al. 2005). Although Didymos is not a Q type, the striking phase curve similarity and shared dynamical properties for both asteroids might indicate that Didymos might have also suffered resurfacing in the past. The phase curve changes when the average particle’s albedo, size distribution, and topography on the asteroid’s uppermost layers are altered. Bright, small, roundish grains translate into less of a steep slope k , while

irregularly shaped darker grains generally lead to steeper slope factors (Hapke 2012). Given Didymos’s diameter range and the possible resurfacing, its surface could be more efficiently depleted of fine submicrometric grains, and this might end up steepening the phase curve slope and broadening the OE through the shadow-hiding effect (Shkuratov et al. 2002). We can also suppose that the process of formation and/or having a secondary body affects such depletion more efficiently.

5. Discussion and Closing Remarks

The phase curve of (65803) Didymos, the target of the DART mission, had not been covered in detail until ground-based observations from the last 20 yr were merged with the presented LUKE RGB observations carried by the ASI/LICIACube. The ground-based observations enable the study

Table 5
The Central Parameters for NEAs with Estimated Geometric Albedo and Diameter

Number (1)	Designation (2)	Rot. Period (3)	Amplitude (4)	Phase Slope k (5)	G1 (6)	G2 (7)	z_{shev} (8)	ρ_v (9)	Diameter (10)	Taxonomy (11)
...	2017 CR32	14.90	0.43	0.0328	0.857	0.133	0.010	0.079	0.16	C
...	2017 DC38	0.0362	0.802	0.000	0.016	0.012	0.20	C
...	2016 WU3	0.0357	0.882	0.019	0.068	0.031	0.73	C
...	2014 AD17	8.48	0.22	0.0213	0.248	0.353	0.305	0.239	0.32	S
...	2005 TF	2.71	0.17	0.0184	0.062	0.147	1.146	0.154	0.59	S
...	2001 UG18	0.0257	0.462	0.330	0.194	0.184	0.24	M
1862	Apollo	3.06	0.13	0.0240	0.380	0.354	...	0.250	1.50	Q
16816	1997 UF9	0.0108	0.000	0.332	0.779	0.292	2.10	S
25143	Itokawa	12.13	1.05	0.0321	0.810	0.158	...	0.270	0.33	S
65717	1993 BX3	20.33	0.83	0.0362	0.966	0.000	...	0.150	0.22	...
99799	2002 LJ3	2.65	0.23	0.0306	0.779	0.221	...	0.430	0.46	Q
101955	Bennu	4.30	0.16	0.0356	0.820	0.019	...	0.044	0.53	B
155140	2005 UD	5.23	0.38	0.0365	0.610	-0.006	...	0.140	1.28	C
159608	2002 AC2	0.0197	0.123	...	0.465	0.200	2.10	S
162173	Ryugu	7.63	0.02	0.0390	0.160	0.040	0.87	C
175189	2005E C224	3.75	0.15	0.0303	0.589	0.181	0.156	0.204	0.75	D
326683	2002 WP	6.26	1.33	0.0109	0.000	0.602	0.328	0.315	0.60	S
333889	1998 SV4	0.0329	0.706	0.107	0.142	0.110	1.20	D
357439	2004 BL86	2.62	0.25	0.0225	0.839	0.400	0.33	V
370307	2002 RH52	4.22	0.36	0.0108	0.000	0.572	0.347	0.363	1.20	E
370702	2004 NC9	7.53	0.52	0.0316	0.818	0.181	0.064	0.091	1.70	D
417581	2006 VA3	5.48	0.40	0.0303	0.769	0.231	...	0.150	0.96	...
464797	2004 FZ1	45.42	0.39	0.0211	0.259	0.383	...	0.100	1.40	S
480004	2014 KD91	2.84	0.17	0.0217	0.261	0.345	...	0.130	1.50	...
484506	2008 ER7	0.0268	0.629	0.371	0.024	0.091	0.44	C

Note. The source of the data is described in the main text.

of the OE regime under varied models. After reconstructing the phase curve for a broad phase angle coverage, we computed the HG1G2 parameters and compared them to a large corpus of asteroid phase curve parameters. Didymos comes out as an unusual S-type asteroid. The OE parameters point to scattering properties in the outskirts of the habitual cluster of S types, skewing toward G/Cg-type asteroids and situated well among M types. On the G1-G2 space, Didymos is placed among the C types, very linear in shape and not displaying the usual broad concavity at phase angles over 25° . One particular model, the linear-by-parts, enables a tentative comparison with meteorite samples and places Didymos among L chondrites. In total, our analysis made use of four varied models in order to provide parameters that can be used for comparison with other asteroid surveys (Muinonen et al. 2022). In addition, such results will be compared with the observations of the upcoming ESA/HERA mission (Michel et al. 2022) that will reach the Didymos–Dimorphos system and study the outcome of the DART experiment at very high spatial resolution.

It is worth noticing that the asteroid trends are built from a database of large asteroids of the main belt. On the contrary, Didymos is a small binary NEA with a diameter of <1 km. In Didymos’s diameter range, processes such as YORP and close planetary encounters can lead to partial resurfacing of the asteroid’s uppermost soil layers (Nesvorný et al. 2005; Marchi et al. 2006; Binzel et al. 2010; DeMeo et al. 2023) and depletion of the majority of fine submicrometric grains (Hsu et al. 2022). Ieva et al. (2022a) and Arcoverde et al. (2023) indeed show that the NEA OE and phase curve morphology can be unusual and diverse from their albedo and spectral types. When Didymos is compared to the phase curve parameters of other NEAs, we observe a similarity to NEA S

types and the asteroid (1862) Apollo, the name-giver of the Earth-crossing dynamical group of which Didymos is a part. The closeness to Apollo might indicate that Didymos has undergone resurfacing processes in the past that could have more efficiently depleted its surface from very fine submicrometric grains.

Didymos’s spectral meteoritic analog in the VIS-NIR range is among the LL ordinary chondrites. It is known that LL ordinary chondrites can display varied degrees of impact melt and/or shock pressuring, geophysical alterations that can darken the albedo and suppress the silicate absorption band in the meteorite structure (Reddy et al. 2014; Kohout et al. 2020). Didymos’s surface may thus be displaying an OE more similar to that expected for the composition of its parent body. The shock darkening or melting might have been produced during the catastrophic impact that gave rise to the ejected material long before it reaccumulated into the Didymos system, or it was already present in the battered parent body.

With data going down to 2.35° phase angle, the three models yield ρ_v ranging between 0.14 and 0.16. This albedo range is $\sim 30\%$ – 45% smaller than the central tendency for asteroids of the S taxonomic complex ($\rho_0 = 0.26 \pm 0.04$; Gustafsson et al. 2019). Even by supposing that Didymos is partially depleted in very fine regolith, similarly to the Hayabusa 2 and OSIRIS-Rex targets Ryugu and Bennu (Grott et al. 2019; Cambioni et al. 2021; Hsu et al. 2022), Bowen et al. (2023) show that at $600 \mu\text{m}$ wavelength, single-scattering albedos of ordinary chondrites do not vary more than 12% when the average grain size changes from 100 to $800 \mu\text{m}$. This effect is $3\text{--}4\times$ weaker than the addition of albedo-suppressing materials. Kohout et al. (2020) show that shock darkening and impact melt may suppress by $\sim 70\%$ the albedo of an ordinary chondrite at

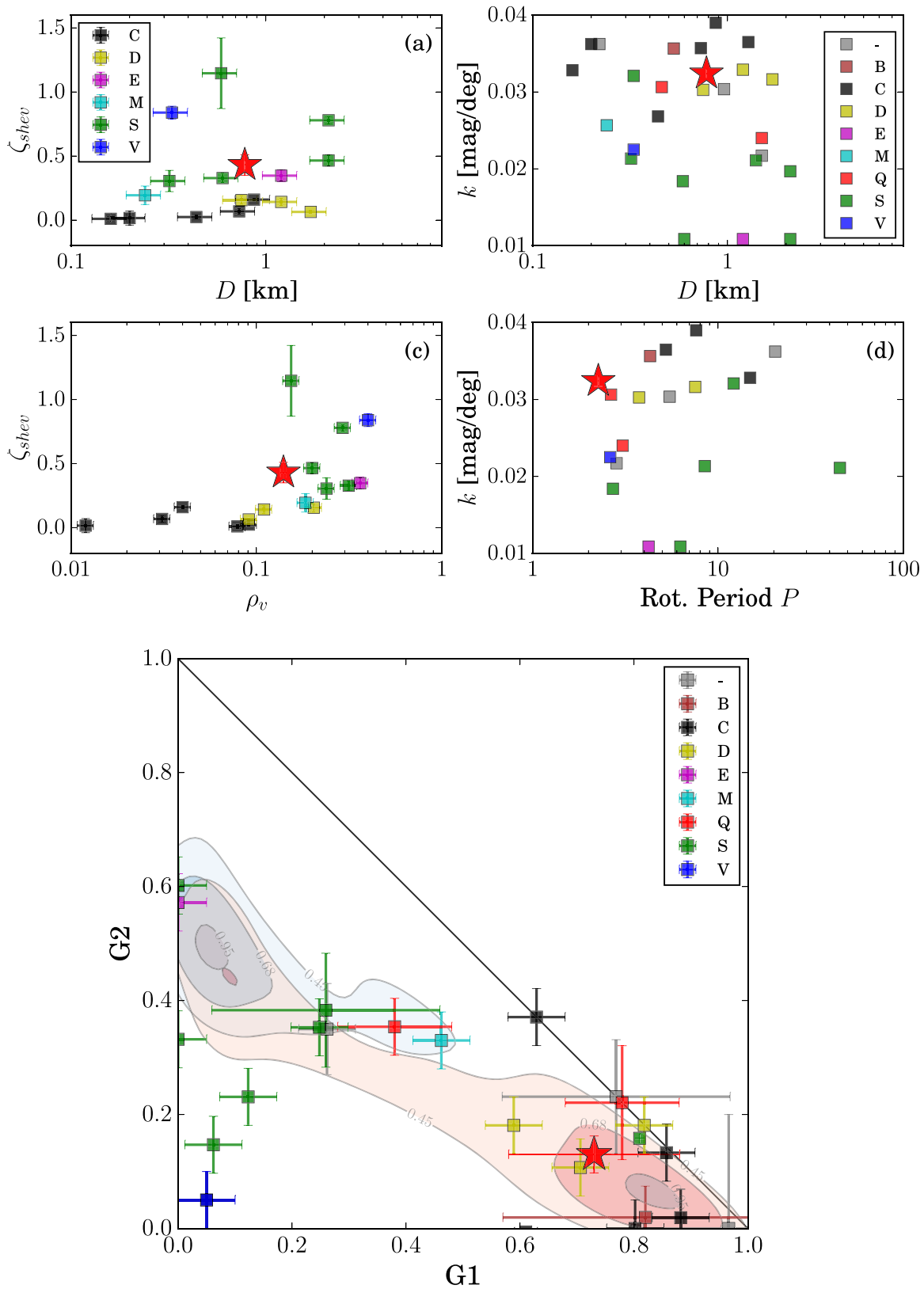


Figure 14. Didymos's phase curve parameters compared to NEA parameters from the literature (see Table 5). The NEAs are color-coded by spectral type. Didymos is represented by a red star. (a) OE amplitude z_{shev} vs. diameter D , (b) phase slope coefficient k vs. diameter D , (c) OE amplitude z_{shev} vs. geometric albedo ρ_v , (d) phase slope coefficient k vs. rotational period P , (e) diagram of G1 vs. G2, with the locus of the S and C types color shaded in the background as shown in Figure 13 (blue and red, respectively).

650 nm. To reduce the average S-type R-band albedo considering only these two darkening agents, Didymos may bear 30%–40% of the shock darkening or 40%–50% of the impact melt. Taxonomically, a silicate asteroid can skew from Q as much as to the C/Ch spectral type through 1 μ m band suppression, given that the original spectrum departs from a fresh nonweathered silicate composition. Very local albedo variation in the darkening agent content can surely be detected by HERA spectroscopic and multiband instruments, such as the Thermal Infrared imager and Hyperscout (Michel et al. 2022). Tracing trends in albedo and color variation are also tools to resolve among various darkening mechanisms (Reddy et al. 2014; Kohout et al. 2020).

Therefore, sampling more phase curves of NEAs could help detect more such unusual compositional cases. In addition, this would also shed light on the question of whether as we get further into smaller asteroids we depart from the usual and expected compositional trends. A hint is given from the ATLAS catalog (Mahlke et al. 2021): we find 47 main-belt S-type asteroids with HG1G2 parameters similar to Didymos.²³ More recently, the NEA (52768) 1998 OR2 came out as a possible candidate for a shock/impact-darkened object (Battle et al. 2022), while radar and phase curve analysis may not confirm the hypothesis (Devoegele et al. 2024).

Alternatively, the similarity of the OE and albedo to the Mezö-Madaras meteorite implies in another possible agent for Didymos darkening, that of unequilibrated L3.7 ordinary chondrites bearing a carbonaceous matrix and graphite inclusions in their Fe-Ni grains (Mostefaoui et al. 1995). Carbon content also acts as an albedo suppressor, which leads to a much darker geometric albedo and shallower silicate bands in the Mezö-Madaras meteorite. The brecciated nature of the meteorite indicates mixing after impact or a larger catastrophic event (Van Schmus 1967). We only cautiously raise this possibility, since Mezö-Madaras's silicate band depths and centers do not match those of Didymos (see NASA Relab Spectrum TB-TJM-079/LATB79 and OC-TXH-004-C/C1OC04C²⁴). Didymos could contain much lesser carbon content and depart from a different silicate bulk composition but undergo a similar albedo effect. Yet, such a particular compositional mixing would require validation from laboratory experiments. We cite, however, Gattacceca et al. (2017), who show the presence of L clasts mixing into an LL ordinary chondrite inside the breccia meteorite Northwest Africa 5764, thus pointing to the possibility of mixing among varied ordinary chondrite types as a veneer of darkening agents as well.

Finally, from 2024 June 20 to July 4 and 2025 October 2 to 22, Didymos will be crossing through the opposition regime as seen from Earth, providing opportunities to improve the geometric albedo estimation and OE characterization and reduce the parametric uncertainties related to limited data points. We also foresee that an in-depth future color analysis based on all three LUKE bands may also shed light on local surface variation and help unveil the properties of Didymos's composition before HERA's arrival.






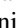












²³ ATLAS at <https://vizier.cds.unistra.fr/viz-bin/VizieR?source=VII/288> (2023 November).

²⁴ RELAB: <https://sites.brown.edu/rehab/rehab-spectral-database/> (2023 November).

Acknowledgments

P.H. thanks Alice Bernard for her help in the revision. P.H. thanks the reviewer C. Feller for his comments that helped improving the final manuscript. P.H. also appreciates the community built around the Python language, as well as their efforts to produce and keep outstanding plotting and statistical packages. This research was supported by the Italian Space Agency (ASI) within the LICIACube project (ASI-INAF agreement AC No. 2019-31-HH.0 CUP F84I190012600). P. P. acknowledges support by the Technology Agency of the Czech Republic, grant 23-04946S. R.T.D., A.S.R., and O.B. were supported by the DART mission, NASA contract No. 80MSFC20D0004.

ORCID iDs

P. H. Hasselmann  <https://orcid.org/0000-0003-1193-8945>
 P. Pravec  <https://orcid.org/0000-0001-8434-9776>
 S. Ieva  <https://orcid.org/0000-0001-8694-9038>
 D. Perna  <https://orcid.org/0000-0002-4545-3850>
 J. D. P. Deshapriya  <https://orcid.org/0000-0002-5758-1286>
 E. Mazzotta-Epifani  <https://orcid.org/0000-0003-1412-0946>
 E. Dotto  <https://orcid.org/0000-0002-9335-1656>
 A. Zinzi  <https://orcid.org/0000-0001-5263-5348>
 G. Poggiali  <https://orcid.org/0000-0002-3239-1697>
 I. Bertini  <https://orcid.org/0000-0002-0616-2444>
 A. Lucchetti  <https://orcid.org/0000-0001-7413-3058>
 M. Pajola  <https://orcid.org/0000-0002-3144-1277>
 M. Dall'Ora  <https://orcid.org/0000-0001-8209-0449>
 J.-Y. Li  <https://orcid.org/0000-0003-3841-9977>
 S. L. Ivanovski  <https://orcid.org/0000-0002-8068-7695>
 A. Rossi  <https://orcid.org/0000-0001-9311-2869>
 J. R. Brucato  <https://orcid.org/0000-0002-4738-5521>
 C. A. Thomas  <https://orcid.org/0000-0003-3091-5757>
 O. Barnouin  <https://orcid.org/0000-0002-3578-7750>
 J. M. Sunshine  <https://orcid.org/0000-0002-9413-8785>
 A. S. Rivkin  <https://orcid.org/0000-0002-9939-9976>
 R. T. Daly  <https://orcid.org/0000-0002-1320-2985>
 E. E. Palmer  <https://orcid.org/0000-0001-6755-8736>

References

- Acton, C., Bachman, N., Semenov, B., & Wright, E. 2018, *P&SS*, 150, 9
 Acton, C. H. 1996, *P&SS*, 44, 65
 Alvarez-Candal, A., Benavidez, P. G., Campo Bagatin, A., & Santana-Ros, T. 2022, *A&A*, 657, A80
 Arcoverde, P., Rondón, E., Monteiro, F., et al. 2023, *MNRAS*, 523, 739
 Battle, A., Reddy, V., Sanchez, J. A., et al. 2022, *PSJ*, 3, 226
 Beck, P., Pommerol, A., Thomas, N., et al. 2012, *Icar*, 218, 364
 Belskaya, I. N., & Shevchenko, V. G. 2000, *Icar*, 147, 94
 Binzel, R. P., Morbidelli, A., Merouane, S., et al. 2010, *Natur*, 463, 331
 Binzel, R. P., Rivkin, A. S., Stuart, J. S., et al. 2004, *Icar*, 170, 259
 Bowell, E., Hapke, B., Domingue, D., et al. 1989, in *Asteroids II*, ed. R. P. Binzel, T. Gehrels, & M. S. Matthews (Tucson, AZ: Univ. Arizona Press), 524
 Bowell, E., & Lumme, K. 1979, in *Asteroids*, ed. T. Gehrels & M. S. Matthews (Tucson, AZ: Univ. Arizona Press), 132
 Bowen, B., Reddy, V., De Florio, M., et al. 2023, *PSJ*, 4, 52
 Cambioni, S., Delbo, M., Poggiali, G., et al. 2021, *Natur*, 598, 49
 Capannolo, A., Zanotti, G., Lavagna, M., et al. 2021, *AcAau*, 182, 208
 Cheng, A. F., Agrusa, H. F., Barbee, B. W., et al. 2023, *Natur*, 616, 457
 Colazo, M., Cabral, J. B., Chalela, M., & Sánchez, B. O. 2022, *A&C*, 38, 100533
 Da Deppo, V., Martellato, E., Rossi, G., et al. 2014, *Proc. SPIE*, 9143, 914344
 Daly, R. T., Ernst, C. M., Barnouin, O. S., et al. 2023, *Natur*, 616, 443
 Daly, R. T., Ernst, C. M., Barnouin, O. S., et al. 2024, *PSJ*, 4, 24

- de León, J., Licandro, J., Duffard, R., & Serra-Ricart, M. 2006, *AdSpR*, **37**, 178
- de León, J., Licandro, J., Serra-Ricart, M., Pinilla-Alonso, N., & Campins, H. 2010, *A&A*, **517**, A23
- Déau, E., Dones, L., Rodriguez, S., Charnoz, S., & Brahic, A. 2009, *P&SS*, **57**, 1282
- Déau, E., Spilker, L. J., & Flandes, A. 2016, *Icar*, **272**, 149
- DeMeo, F. E., Marsset, M., Polishook, D., et al. 2023, *Icar*, **389**, 115264
- Deshapriya, J. D. P., Hasselmann, P. H., Gai, I., et al. 2023, *PSJ*, **4**, 231
- Devogele, M., McGilvray, A., MacLennan, E., et al. 2024, *PSJ*, **5**, 44
- Dotto, E., Della Corte, V., Amoroso, M., et al. 2021, *P&SS*, **199**, 105185
- Dotto, E., Deshapriya, J. D., Gai, I., et al. 2024, *Natur*, in press
- Dunn, T. L., Burbine, T. H., Bottke, W. F., & Clark, J. P. 2013, *Icar*, **222**, 273
- Fairbairn, M. B. 2005, *JRASC*, **99**, 92
- Fletcher, Z. J., Ryan, K. J., Ernst, C. M., et al. 2022, *Proc. SPIE*, **12180**, 121800E
- Gattacceca, J., Krzesińska, A. M., Marrochi, Y., et al. 2017, *M&PS*, **52**, 2289
- Grott, M., Knollenberg, J., Hamm, M., et al. 2019, *NatAs*, **3**, 971
- Gustafsson, A., Trilling, D. E., Mommert, M., et al. 2019, *ApJ*, **158**, 67
- Hapke, B. 1993, *Topics in Remote Sensing* (Cambridge: Cambridge Univ. Press)
- Hapke, B. 2012, *Theory of Reflectance and Emittance Spectroscopy* (2nd ed.; Cambridge: Cambridge Univ. Press)
- Harris, A. W., & Lagerros, J. S. V. 2002, in *Asteroids III*, ed. W. F. Bottke, Jr. (Tucson, AZ: Univ. Arizona Press), 205
- Hasselmann, P. H., Barucci, M. A., Fornasier, S., et al. 2016, *Icar*, **267**, 135
- Hasselmann, P. H., Fornasier, S., Barucci, M. A., et al. 2021, *Icar*, **357**, 114106
- Hergenrother, C. W., Maleszewski, C. K., Nolan, M. C., et al. 2019, *NatCo*, **10**, 1291
- Hoffman, M. D., & Gelman, A. 2014, *J. Mach. Learn. Res.*, **15**, 1593
- Hsu, H.-W., Wang, X., Carroll, A., Hood, N., & Horányi, M. 2022, *NatAs*, **6**, 1043
- Huang, J. N., Muinonen, K., Chen, T., & Wang, X. B. 2021, *P&SS*, **195**, 105120
- Ieva, S., Arcoverde, P., Rondón, E., et al. 2022a, *MNRAS*, **513**, 3104
- Ieva, S., Mazzotta Epifani, E., Perma, D., et al. 2022b, *PSJ*, **3**, 183
- Ishiguro, M., Kuroda, D., Hasegawa, S., et al. 2014, *ApJ*, **792**, 74
- Joye, W. A. 2006, in *ASP Conf. Ser. 351, Astronomical Data Analysis Software and Systems XV*, ed. C. Gabriel et al. (San Francisco, CA: ASP), 574
- Kaasalainen, S., Piironen, J., Kaasalainen, M., et al. 2003, *Icar*, **161**, 34
- Kitazato, K., Abe, M., Mito, H., et al. 2004, *LPSC*, **35**, 1623
- Kohout, T., Penttilä, A., Mann, P., et al. 2020, *PSJ*, **1**, 37
- Lederer, S. M., Domingue, D. L., Thomas-Osip, J. E., et al. 2008, *EP&S*, **60**, 49
- Li, J. Y., Helfenstein, P., Buratti, B., Takir, D., & Clark, B. E. 2015, in *Asteroids IV*, ed. P. Michel, F. E. DeMeo, & W. F. Bottke (Tucson, AZ: Univ. Arizona Press), 129
- Lumme, K., & Bowell, E. 1981, *AJ*, **86**, 1694
- Lumme, K., & Irvine, W. M. 1976, *AJ*, **81**, 865
- Lupton, R., Blanton, M. R., Fekete, G., et al. 2004, *PASP*, **116**, 133
- Mahlke, M., Carry, B., & Denneau, L. 2021, *Icar*, **354**, 114094
- Marchi, S., Magrin, S., Nesvorný, D., Paolicchi, P., & Lazzarin, M. 2006, *MNRAS*, **368**, L39
- Mazzotta Epifani, E., Dall’Ora, M., Dotto, E., et al. 2023, in *Asteroids, Comets, Meteors Conf.*, 2388
- Menon, D., Andriani, S., & Calvagno, G. 2007, *ITIP*, **16**, 132
- Michel, P., Küppers, M., Bagatin, A. C., et al. 2022, *PSJ*, **3**, 160
- Mostefaoui, S., Perron, C., Chaussidon, M., Hanon, P., & Robert, F. 1995, *Metic*, **30**, 553
- Muinonen, K., Belskaya, I. N., Cellino, A., et al. 2010, *Icar*, **209**, 542
- Muinonen, K., Penttilä, A., Cellino, A., et al. 2009, *M&PS*, **44**, 1937
- Muinonen, K., Uvarova, E., Martikainen, J., et al. 2022, *FrASS*, **9**, 821125
- Nesvorný, D., Jedicke, R., Whiteley, R. J., & Ivezić, Ž. 2005, *Icar*, **173**, 132
- Ostro, S. J., Benner, L. A. M., Giorgini, J. D., et al. 2005, *IAUC*, **8627**, 2
- Palmer, E. E., Barnouin, O. S., Daly, R. T., et al. 2023, in *Asteroids, Comets, Meteors Conf.*, 2466
- Palmer, E. E., Gaskell, R., Daly, M. G., et al. 2022, *PSJ*, **3**, 102
- Park, W., Pak, S., Shim, H., et al. 2016, *AdSpR*, **57**, 509
- Penttilä, A., Shevchenko, V. G., Wilkman, O., & Muinonen, K. 2016, *P&SS*, **123**, 117
- Poggiali, G., Brucato, J. R., Hasselmann, P. H., et al. 2022, *PSJ*, **3**, 161
- Pravec, P., Benner, L. A. M., Nolan, M. C., et al. 2003, *IAUC*, **8244**, 2
- Pravec, P., & Harris, A. W. 2007, *Icar*, **190**, 250
- Pravec, P., Scheirich, P., Kušnirák, P., et al. 2006, *Icar*, **181**, 63
- Pravec, P., Thomas, C. A., Rivkin, A. S., et al. 2022, *PSJ*, **3**, 175
- Rabinowitz, D. L. 1991, *AJ*, **101**, 1518
- Reddy, V., Gary, B. L., Sanchez, J. A., et al. 2015, *ApJ*, **811**, 65
- Reddy, V., Sanchez, J. A., Bottke, W. F., et al. 2014, *Icar*, **237**, 116
- Scheirich, P., & Pravec, P. 2022, *PSJ*, **3**, 163
- Seabold, S., & Perktold, J. 2010, in *Proc. of the 9th Python in Science Conf.*, ed. S. van der Walt & J. Millman (Austin, TX: SciPy), 96
- Shevchenko, V. G. 1996, *LPSC*, **Vol. 27**, 1193
- Shkuratov, Y., Kaydash, V., Korokhin, V., et al. 2011, *P&SS*, **59**, 1326
- Shkuratov, Y., Ovcharenko, A., Zubko, E., et al. 2002, *Icar*, **159**, 396
- Stuart, J. S., & Binzel, R. P. 2004, *Icar*, **170**, 295
- Thomas, C. A., Naidu, S. P., Scheirich, P., et al. 2023, *Natur*, **616**, 448
- Van Schmus, W. R. 1967, *GeCoA*, **31**, 2027
- Vereš, P., Jedicke, R., Fitzsimmons, A., et al. 2015, *Icar*, **261**, 34